Title

Mechanical stretching can modify the axial morphology of early chick embryos

Author list

Ben K.A. Nelemans[1*], Manuel Schmitz[1*], Hannan Tahir[1,2], Roeland M.H. Merks[2,3], Theodoor H. Smit[4,5]

* These authors contributed equally to this work.

Corresponding author is Theodoor H. Smit (t.h.smit@amc.nl)

Affiliations

1 Department of Orthopaedic Surgery, VU University Medical Center, Amsterdam Movement Sciences, Amsterdam, The Netherlands

2 Centrum Wiskunde & Informatica, Amsterdam, The Netherlands

3 Mathematical Institute, Leiden University, Leiden, The Netherlands

4 Department of Medical Biology, Academic Medical Center, Amsterdam, The Netherlands

5 Amsterdam Movement Sciences Research Institute, The Netherlands

Abstract

Vertebrates are characterized by their segmented structure, first visible in the somites that form along the embryonic body axis. Somites are the predecessors of the vertebrae, ribs, muscles and the skin and impose a segmented organization on the peripheral nervous system. The variability in somite number between species has presumably evolved by genetic rearrangements, leading to changes in the ratio of the segmentation clock rate to the developmental growth rate. However, it is known that physical cues, like temperature, salinity or light conditions, can modify the vertebrate body plan and change the vertebral number. Here we show that mechanical stretching, another physical cue, can induce the formation of additional somites in the developing chicken embryo. Stretching of live chick embryos and the resulting deformation of somites induces a slow cellular reorganization of somites to form two or more well-shaped and stable daughter somites. Mesenchymal cells from the somite core thereby undergo mesenchymal-to-epithelial transitions (MET), thus meeting the geometrical demand for more border cells. Our simulations, using a Cellular Potts Model of somite remodeling, suggest that this MET occurs through lateral induction by existing epithelial cells. Our results strengthen the idea that somitic mesoderm self-organizes, and show that it is phenotypically plastic under variations in the mechanical environment. These somite qualities could play out as a selective advantage by preventing the formation of transitional vertebrae and give rise to another possibility how the vertebrate body axis might have evolved towards different vertebral numbers, next to the previously proposed genetic rearrangements.

INTRODUCTION

A segmented spine is the characteristic feature of the vertebrate body plan: it provides mechanical support, flexibility, and protection of the spinal cord. While the ground form of vertebrae and indeed their function are well conserved throughout the phylum, their number varies considerably among species, ranging from six in the frog to several hundred in snakes (1). The evolvability of the vertebral column allows vertebrates to adapt to diverse habitats and acquire matching locomotor styles by tuning the number of body segments (2).

Patterning of the vertebrate body originates early in embryogenesis when the paraxial mesoderm on both sides of the midline segments into somites, the predecessors of the vertebrae. Somites are cell blocks in which an epithelial layer surrounds a core of mesenchymal cells, the somitocoel (3, 4). The sequential partitioning of the paraxial mesoderm appears to be imposed by a molecular clock and a travelling wave of maturation, created by a system of signaling gradients (5). The clock and wavefront form a complex signaling network that appears well conserved throughout the vertebrate phylum. The different somite numbers observed in different species are presumably due to mutations that lead to changes in the speed of the clock or the elongation rate of the mesoderm, which both affect segmentation rate and somite size (6).

Despite the intricately controlled network of the clock-and-wavefront mechanism, environmental cues, like temperature, salinity or the light conditions during early embryonic development can influence the vertebral number significantly in fish (7–9), amphibians (10, 11), reptiles (12), mammals (13) and birds (14). Mechanics could be another physical cue to induce different phenotypes of segmental patterning. In the framework of the Extended Evolutionary Synthesis, it

has been argued by the ‘side effect hypothesis’ that morphological novelties in the body plan can also occur as a result of changing mechanical cues exerted on self-organizing developing tissues, aside genetic rearrangements (15–17). Somitic tissue possesses a certain capacity for self-organization, as somite-like structures can form ectopically in the absence of a clock or a wavefront (18). The size of epithelializing somites strongly correlates with embryonic growth (19) and hampering axial elongation of the embryo leads to disorganized somites (20). Furthermore, somite formation requires the contraction of cells in the PSM (21) and mechanical adhesion to the surrounding fibronectin matrix (4, 22).

Based on these observations, we hypothesized that if somitic mesoderm self-organizes under influence of biomechanical cues, mechanical stretching should then suffice to induce morphological changes in the segmented vertebrate body plan. To test this hypothesis, we developed a novel experimental setup to apply controlled strains to live chick embryos. Time-lapse movies were made which confirmed that mesodermal patterning indeed can be modulated given sufficient strain (Fig. S1). This suggests that mechanical cues can affect morphogenesis and may be an explanatory factor for variation in vertebral numbers in the scope of the side effect hypothesis.

RESULTS

Mechanical stretching can induce a slow cellular reorganization of somitic tissue into “daughter somites”

To test the effect of mechanical stretching on somitogenesis, stage HH8-9 chick embryos (23) were cultured *ex ovo* in modified submerged filter paper sandwiches (24) and stretched along their body axis in two intervals at 1.2 µm/s (Fig. S1). As a result, the embryos experienced strain values of 23

± 3% (average ± SD) after the first pull and 19 ± 3% after the second pull. Approximately 12 hours after manipulation, one third (19/57) of all stretched embryos showed single or multiple incidents of disturbed mesodermal segmentation compared to control embryos of the same age (Fig. 1A and B). Time-lapse microscopic imaging (24) revealed that somites budded off from the PSM at regular intervals of 79 ± 8 minutes in controls and 80 ± 6 minutes in stretched samples. Stretched somites were heavily elongated as compared to somites in control embryos (Fig. 1C-F, Movie S1 and Movie S2). These deformed somites then regularly divided into what we call "daughter somites", in accordance with somite divisions observed in N-cadherin and Cadherin-11 knockout mice (25, 26). During daughter somite formation, an invagination along the mediolateral plane of the deformed somites appeared, simultaneously to their separation from the PSM (Fig. 1F, Movie S2). It took several hours from the first appearance of this mediolateral invagination for the somite to divide completely. Somite division in stretched embryos appeared uni- or bilaterally and often resulted into daughter somites of different sizes (Movie S2, Fig. S4, Fig. S5 and Fig. S8).

Mesenchymal cells from the somite core epithelialize and get incorporated into the somitic epithelium during daughter somite formation

Daughter somites appeared as stable, rounded and clearly separated cellular spheres (Fig. 1B). They were morphologically similar to control somites: epithelial cells were organized radially around a somitocoel of mesenchymal cells (compare Fig. 2C and G). The daughter somites were enclosed by a fibrous extracellular matrix (ECM), staining positively for fibronectin (Fig. S4). While somites in control embryos were rounded (Fig. 2A), somites in stretched embryos were elongated while any daughter somites were variable in size (Fig. 2B, Fig. S4 and Fig. S5). Small daughter somites, consisting of a few epithelial cells only, were also observed (Fig. S4). The apical actin cortices of somites, fixated in transitional stages, showed discontinuities along their mediolateral plane,

indicating openings of the epithelial sheet under influence of the mechanical deformation (Fig. 2D, E and Fig. S6). At these locations, mesenchymal somitocoel cells appeared elongated, presumably underwent a mesenchymal-to-epithelial transition (MET) and were integrated into the existing epithelium (Fig. 2E and Fig. S6). This was accompanied by a strong ectopic expression of *EphA4* in the somitocoels upon stretching (Fig. 2I), which was not present in control embryos (Fig. 2H), indicative of stretch-induced MET. During normal somitogenesis, cell-cell signaling by receptor EphA4 in the rostral part of somite S-I (and its ligand ephrin B2 in the caudal half of somite S0) does not only induce formation of the somite gap (27), but also establishes epithelialization at somite boundaries by initiating a columnar morphology and cell polarity via apical redistribution of β-catenin (28).

The mechanical stimulus did not change the genetic patterning of the unsegmented PSM (Fig. 2J-M): the expression pattern for *cMeso1,* the key initiator of somite rostro-caudal polarity in chicken (29), was not influenced by the stretching (Fig. 2K), and the expression pattern of caudal somite marker *Uncx4.1* (30) showed that daughter somites did not gain a new rostro-caudal genetic identity (Fig. 2M). Altogether our data suggests that mechanical stretching did not affect the unsegmented PSM or the rostrocaudal polarization of the somites. However, mechanical stretching did lead to continuation of EphA4-mediated epithelialization of mesenchymal cells from the somitocoel in the newly segmented PSM.

Cellular Potts model of somite division suggests a contact-induced epithelialization mechanism during daughter somite formation

We next explored under which conditions mechanically deformed somites would successfully reorganize into daughter somites. To this end, we developed a cell-based computer simulation

based on the Cellular Potts model (CPM) (32), for which we used the open source package CompuCell3D (33). The somite consisted of a core of non-polarized mesenchymal cells surrounded by a layer of polarized, epithelial cells (18). We simulated a somite embedded within an elastic extracellular matrix (ECM; Fig. 3A) and mimicked stretching by applying axial tension to the ECM (Fig. 3B, Movie S3). We tested different rules for cellular behavior in the deformed somite (Fig. S10) to narrow down the possible mechanisms for somite reorganization under mechanical deformation. Daughter somite formation *in silico* could successfully be induced only if MET was initiated when mesenchymal core cells came into contact with the basal or lateral membranes of epithelial cells (Fig. 3C, C' and D). To validate this model prediction, we calculated the relative fraction of mesenchymal and epithelial cells in the equatorial cross-section of control somites and divided somites. We found that the epithelial cell fraction was indeed significantly increased in daughter somites compared to controls, *in vivo*. This matched the *in silico* prediction, independent of the size of the initial somite (Fig. 3E, Fig. S11). We could not detect significant changes in apoptosis/proliferation rate due to the stretching *in vivo* (Fig. 3F). Therefore, the increase of the epithelial cell fraction must be due to MET. To determine the relation between mechanical deformation and somite division, we measured the aspect ratios of stretched dividing somites (prior to division) and stretched non-dividing somites compared to control somites (Fig. 3G, Fig. S7). These measurements show that somite division is only possible beyond an aspect ratio threshold of about 2 *in vivo* or 2.5 *in silico*. The corresponding receiver operating characteristics (ROC) curves (34–37) show that the somite aspect ratio is indeed an excellent predictor of somite division *in vivo* and *in silico*, indicating that daughter somite formation is a highly mechanically determined process (Fig. 3H).

DISCUSSION

Somitic mesoderm organization can be modified by physical changes in its environment

We found that mechanical stretching of live chick embryos can induce a slow reorganization of somites to form two or more well-shaped and stable daughter somites. The complete division of a stretched somite into daughter somites took several hours, indicating that daughter somite formation is an active process of tissue reorganization, rather than acute mechanical disruption. The resulting formation of new epithelial borders happened in the somitic mesoderm, *i.e.* outside the functional range of the molecular cues described in the clock-and-wavefront mechanism (5). Apparently, newly forming somites can continuously adapt to changes of their environment and their organization is not definite upon their separation from the anterior tip of the PSM. Similarly, it has been shown before that the development of the somitic epithelia involves a continuous addition of cells from the somitocoel by accretion and egression (4). Our observations indicate that this dynamic cellular behavior actively adds mesenchymal cells to the epithelium during stretching; the epithelium thereby adapts to the changing environment, leading to daughter somite formation under sufficient deformation. In the future, it would be interesting to study the effect of modified mesodermal patterning in stretched embryos on later embryonic development (e.g. the organization of the nervous system and vertebral numbers). Although *ex ovo* cultured embryos can successfully be transplanted back into a host egg (38), in our case this could prove technically challenging because the stretched embryos are significantly deformed. Therefore, it could prove more promising to transplant daughter somites into host chick embryos in the egg and see how skeletal patterning might be influenced.

MET during daughter somite formation

High-resolution confocal imaging revealed discontinuities in the apical actin cortex of stretched somites. This created a direct contact interface between cells of the somitic epithelium and the mesenchymal cells in the somite core. As a result, the mesenchymal cells underwent mesenchymal-epithelial transition (MET) and were recruited into the existing epithelium, similar to the accretion process during normal somite formation (4). In this way, the demand for additional border cells during daughter somite formation could be satisfied. Under sufficient strain and partial opening of its epithelial layer, a somite then divides into daughter somites by reorganizing its epithelial cells and integrating additional mesenchymal cells into the existing epithelium. Two observations strike us: first, the ongoing *EphA4* expression is seen without c*Meso1* expression in the strained somites, where *EphA4* is thought to be downstream of c*Meso1* (27). This indicates that *EphA4* expression is maintained. Alternatively, it might be reinitiated in stretched somites, suggesting an additional mechanosensitive pathway leading to *EphA4* upregulation during somite division, independent from or redundant to c*Meso1*. Second, the segmentation clock speed and segmentation stay robust during the severe deformation imposed on the embryo. A possible explanation for this is that the FGF/WNT gradients are intracellular by mRNA or protein inheritance (39) and therefore cells retain the local information, although spaced differently.

A contact-induced MET mechanism and epithelial self-organization

We could model daughter somite formation *in silico* only if MET was initiated when mesenchymal core cells came into contact with the basal or lateral membranes of epithelial cells. Together with the ectopic upregulation of *EphA4* in stretched somitic tissue, this suggest a contact-induced mechanism triggering MET of somitocoel cells during daughter somite formation. *In vivo*, such a contact-induced MET mechanism could underlie the epithelial self-organization during formation

and homeostasis of epithelia under mechanical stress (4, 40). This cell behavior could be mediated via epithelial membrane-based signaling (41, 42), for example based on the level of Eph and ephrin binding.

The implications of somite plasticity and self-organization for vertebrate body development and evolution

Our data reveal that chick somites are phenotypically plastic under changing biomechanical conditions. Daughter somite formation is highly mechanically determined as the geometry of a somite in a stretched embryo predicts with remarkable reliability if it will reorganize into daughter somites or not. This supports the idea that mechanics could function as an additional cue to the induction of different phenotypes of segmental patterning during embryonic development, in addition to temperature, light regime or salinity (9). Therefore, our data provide a good basis for further exploration into the causal role of mechanics in morphogenesis and body plan evolution.

In perspective of the side effect hypothesis (17), one can imagine that natural selection acting on body proportions may have changed the geometry or the mechanical loading of the somitic mesoderm. A correlation between axial growth of the embryo and somite size has been shown in mice (19). The phenotypic plasticity of somites that we show in our experiments then might lead to deviating somite numbers as an initial by-product. Maintenance of a consistent alteration of the somite number over generations may then later become consolidated at the gene level by natural selection via genetic assimilation (43, 44), thus giving robustness to the development of the newly acquired body plan. As the daughter somites do not generate new somite polarity (Fig. 2M), new segments induced via this plasticity might have fused parts of their vertebrae or ribs (45), but can be useful as a source of skeletal variation for selection to act on.

The observed plasticity of somites and their tendency to self-organize into spherical cell clusters might play a crucial role in maintaining the functionality of the vertebral column by suppressing the occurrence of transitional vertebrae, as observed in many amniote species, including certain species of *Triturus* newts and skinks. Species with an increased number of trunk vertebrae also had a larger intraspecific variation in the number of trunk vertebrae (up to four in *Triturus* species). However, transitional vertebrae, i.e. vertebrae with morphological characteristics of two adjacent regions (for example trunk and sacrum) are statistically underrepresented in these species. This suggests a developmental mechanism favouring complete numbers of trunk vertebrae, rather than transitional vertebrae that might hamper mechanical function (46, 47). If additional trunk somites would form bilaterally via daughter somite formation, both newly created somites might have the same axial identity as their mother somite, given that the Hox identity is determined mainly before the somite is formed, during the earliest stages of somite formation (48–50). This would generate vertebrae of a similar regional identity that mechanically function adequately, compared to potentially disadvantageous transitional vertebrae with a different morphology. A similar mechanism might form the basis for the underrepresentation of transitional vertebrae in lizards. This might explain how high intraspecific and intersexual variations of vertebral numbers can be associated with unexpectedly small frequencies of transitional vertebrae ((51), personal communications with Frietson Galis).

The qualities of chick somitic mesoderm to self-organize into discrete cell clusters and to adjust their size by mechanical environmental influences, thus, could be of selective advantage by preventing the formation of transitional vertebrae. As a side effect, these qualities can facilitate the increase in number of somites when the mechanical environment of the somitic mesoderm changes.

Our data therefore give rise to another possibility how the vertebrate body axis might have evolved towards different vertebral numbers, next to the previously proposed genetic rearrangements (6).

MATERIALS AND METHODS

Egg handling

Fertilized chicken eggs, white-leghorn, *Gallus gallus domesticus* (Linnaeus, 1758), were obtained from Drost B.V. (Loosdrecht, The Netherlands), incubated at 37,5°C in a moist atmosphere, and automatically turned every hour. After incubation for approx. 33 h, embryos were explanted using filter paper carriers (52) and cultured *ex ovo* as modified submerged filter paper sandwiches (24, 52)

Culture medium

Embryo culture medium consisted of Pannett-Compton (PC) saline (24, 53, 54), mixed with freshly harvested thin albumen in a 3:2 ratio. PC stock solutions can be stored at 4 ^{0}C for several months, but PC saline (mixture of stock solutions and MilliQ-water) should be prepared freshly every week and stored at 4^{0}C between experiments. Addition of Penicillin/Streptomycin (10000 U/ml) in 100x dilution prevents occasionally appearing bacterial infections.

Silicone sheets

Silicone sheets protected embryos in culture from convection of the medium, thereby avoiding additional damage. Silicone sheets (ca. 350 µm in thickness) were made using a Sylgard® 184 Silicone Elastomer Kit as follows: A 15-cm plastic petri dish was placed on a scale and 6.165 g (5.554 mL) of base solution were pipetted into its center using a plastic transfer pipette (cut off tip). Then 0.206 g (0.2 mL) of curing agent were added using a glass pipette. Base and curing agent were mixed slowly, using a wooden spatula and spread out over the bottom of the petri dish. The petri dish was placed into a vacuum chamber for 2 hrs to remove air bubbles and let silicone

solution spread out equally. Exposure to 80 °C for ca. 2 hrs let silicone polymerize and cure. Afterwards, silicone was let to cool to room temperature for about 5 hrs or overnight. Tweezers were used to free the borders of the silicone sheet from the walls of the petri dish and peel the sheet from the culture dish (wear gloves). Silicone was stored between sheets of a plastic document sleeve to prevent accumulation of dust. For preparing silicone sheets fitting in the setup, the plastic sleeve was removed from one side of the silicone sheet and the plastic stencil (Fig. S1D) placed on it. A razor blade was used to cut around the outline of the stencil and the ten holes indicated by the stencil were cut out using a hole puncher. After removing the other plastic sleeve layer, silicone sheets were stored in a closed 10 cm petri dish.

Filter paper carriers

Filter paper carriers were prepared as described recently (24). Additionally, four holes were cut out from corners of the carriers (Fig. S1C) to hook the filter paper sandwiches onto the pins of the motorized arms of the stretching setup (Fig. S1A).

Experimental setup/ Embryo stretcher

Embryos were cultured and mechanically manipulated on a custom-made embryo stretcher (Fig. S1C). This setup allows to culture up to three embryos simultaneously in a variant of the recently described "submerged filter paper sandwich" (24). The setup consisted of a temperature-controlled medium container/ beaker surrounded by a metal frame. This frame carried two motorized translation stages mounted on opposing sides of the frame. Both stages could be operated with a manual controller. For one of the stages the control could be switched to a custom-made LabVIEW routine. This routine allowed to define different automated pulling profiles for overnight experiments (see section 'Stretching protocol'). Each stage carried a metal arm reaching into the

medium container. Each metal arm ended with a horizontal platform equipped with three arrays of four smooth pins surrounding a threaded pin. The smooth pins functioned as hooks for the filter paper sandwiches and as a guide for metal washers clamping the filter paper sandwiches to the metal arms. Embryos were cultured fully submerged in the culture medium described above and the setup was prepared for an experiment as follows: The temperature-controlled beaker was placed in the center of the motorized x-y-stage of the upright zoom microscope. Then the frame carrying the two motorized translational stages was placed around the temperature-controlled beaker and fixed it with two lateral screws (Fig. S1B). The two metal arms were attached to the motorized translational stages and fixed with the screws from top. Using the manual control, the position of the metal arms was adjusted so that the gap between them was 12 mm, by bringing the left translational stage furthest to the right and the right translational stage furthest to the left. Then the temperature controlled beaker was filled with 200 mL of clean culture medium. Any dirt or bubbles were removed from the culture medium using a plastic transfer pipette. If necessary, the culture medium level was adjusted to make sure that the pins on the metal arms were just submerged. The temperature of the temperature-controlled beaker was set to 40°C.Then the silicone sheets were placed into the setup by using the blunt end of tweezers to hook the silicone sheets into the pins of the metal arms. Air bubbles were removed with a plastic transfer pipette. Then a chick embryo was explanted into a filter paper sandwich (24) (Fig. S1A), immediately submerged into the culture medium and hooked it into the innermost pins of both metal arms by pushing it down with the tweezers (Fig. S1A The metal washers (Fig. S1A and Fig. S1E for dimensions) were placed over the pins of both metal arms and gently fixed by nuts using an Inbus® key (Fig. S1A). After successfully clamping three filter paper sandwiches into the setup, each filter paper sandwich was cut perpendicularly to the embryonic axis, about 1 mm posteriorly of the widest point of the elliptical aperture (dashed red line in Fig. S1A-9). Iris scissors were used for these cuts. Then the

surface of the culture medium was covered with 50 mL of light mineral oil using a plastic transfer pipette (Fig. S1A-10). Note: After placing the mineral oil, the experiment is set and embryos cannot be replaced anymore without cleaning the whole setup. 25 mL of culture medium were removed from below the oil layer by pinching a plastic transfer pipette through the oil layer into the culture medium and the time-lapse acquisition was set up as described before (24).

Stretching protocol

Embryos were exposed to a standardized stretching protocol which, in preliminary experiments, had proved to cause a strong deformation of the embryos' paraxial mesoderm without impairing the progression of development. The protocol started with a waiting period of 3.5 hrs after covering the culture medium with light mineral oil. This allowed damage, caused during preparation of the filter paper sandwich and perpendicular cutting, to heal. Then, two consecutive stretching intervals followed, separated by a pause of two hours to allow recovery of damaged tissue. Each stretching interval consisted of a slow displacement of the computer controlled metal arm (see red arrow in Fig. S1) by 3.7 to 3.95 mm at a speed of 1.2 µm/s. At this speed, each stretch took 53 to 55 min. Fig. S2 depicts the user interface of the LabVIEW routine, prepared for an overnight experiment. Travel direction (left or right), speed (to be chosen from a 16-bit range defined by the microcontroller, where 40 equals 1.2 µm/s) and time interval (in seconds) could be chosen independently for each experimental block.

Macroscopic axial deformation

The macroscopic axial deformation of the stretched embryos was determined by measuring their length from tip of the head to the posterior end of the sinus rhomboidalis, using the segmented line tool in ImageJ (white line in Fig. S3A, B, E, F). We assumed that, during the application of the

stretching, the natural morphogenetic changes of the embryos are negligible and length changes result from the external stretching only. We calculated the mechanical strain for the first and the second stretching as relative length change compared to the axial length before stretching. Results are presented in S1 Table. The first stretch lead to 23 ± 3 % strain (average and standard deviation over all 21 embryos presented in S1 Table). The second pull caused 19 ± 3 % strain.

Somite formation time

The separation of a newly forming somite from the anterior tip of the PSM and its epithelialization is a continuous process involving complex cellular rearrangements lasting longer than the 90 min usually stated to be characteristic for chick embryos (4). Nevertheless, we tried to assess the influence of mechanical deformation on somitogenesis by determining an average somite formation rate for stretched and control embryos using our dark field microscopic time-lapse movies and based our calculations on the physical separation of somites from the PSM. We counted the number of somites in stretched embryos at the end of the second pull and at the end of the experiment. If a somite had not completely separated from the PSM at the end of the second pull, the counting was started after formation of the following somite. From the total number of somites formed after the application of the second pull and the corresponding time interval we calculated the somite formation rate. The somite formation rate for control embryos was determined accordingly from the beginning of the culturing in the submerged filter paper sandwich. We did not observe any difference in somite formation rate between stretched embryos with or without daughter formation or in comparison to non-stretched control embryos (S2 Table).

Immunohistochemistry

After the pulling experiments, the embryos and age-matched controls were fixed in 4% paraformaldehyde overnight in phosphate buffered saline (PBS) at 4ºC. Permeabilization in PBST + 0.15% Triton-X-100 lasted for 1.5 hours. Blocking was performed for 2 hours in PBST + 2% BSA + 5% normal goat serum. The following antibody was used: fibronectin mouse-anti-chicken (B3/D6-s, Hybridoma bank). The antibody was diluted in PBST with 1% BSA. Embryos were incubated in primary antibody solution for 24h at 4ºC, followed by extensive washing in PBS and incubation with appropriate Alexa Fluor-conjugated secondary antibody (1:500, Molecular Probes). Embryos were stained for F-actin using Alexa Fluor 546 Phalloidin (1:200, Molecular Probes) and for nucleic DNA using DAPI (1 µg/ml).

Cell proliferation and apoptosis staining

Embryos were prepared as described above and immunohistochemistry was performed using following antibodies: rabbit polyclonal anti-cleaved caspase-3 (1:200, Cell Signaling) and rabbit polyclonal anti-phosphohistone-H3 (1:400, Cell Signaling) with the appropriate Alexa Fluor-conjugated secondary antibodies (1:500, Invitrogen) and DAPI for nucleic DNA (1 µg/ml).

***In situ* hybridizations**

In situ hybridizations were performed by standard procedures. Embryos were fixated in freshly prepared 4 % PFA in PBS. The embryos were pretreated with proteinase-K in PBST at 37°C with agitation for 3 minutes. During staining, embryos were incubated in NTMT containing 4.5 µl NBT (75mg/ml in 70% DMF) and 3.5 µl BCIP (50mg/ml in 100% DMF) per 1.5 ml. Pulled embryos and age-matched controls were stained in the same wells for the same time, as much as possible.

After the staining had been stopped, the embryos were photographed in glycerol 80% in H_2O with a Leica DFC320 camera on a Leica MZ75 microscope.

Proliferation rate and apoptotic rate

Apoptotic (Cas3 staining, control n=4, pulled n=4 embryos) and proliferating (pHH3 staining, control n=6, pulled n=6 embryos) cells in somitic mesoderm lanes (somite S1 to S5) were counted in high-resolution confocal micrographs acquired on a Leica SP8 confocal microscope. At least 500 cells were counted per embryo. Apoptotic rate and proliferation rate were calculated as follows: (apoptotic/proliferation) rate (%) = number of positive staining cells/number of total cells×100. Statistical analysis was performed using GraphPad Prism software. Mann–Whitney unpaired non-parametric two-tail testing was applied to determine the P-values for the apoptotic and proliferation rates shown in Fig. 3F. Control and pulled somitic mesoderm showed no significant differences in apoptotic (P=0.4286) and proliferation (P=0.7879) rates.

Epithelial cell percentages

The percentage of epithelial cells in the equatorial z-plane of 13 daughter somite pairs, originating from the same mother somite, and 22 control somites was determined (*in vivo).* To that end, high-resolution confocal micrographs of embryos stained with DAPI for nucleic DNA were acquired on a Leica SP8 confocal microscope. Then somites were counted for (mesenchymal) core cells and epithelial cells to calculate epithelial cell percentages. *In silico,* cell percentages in 12 daughter somite pairs and 12 control somites were counted accordingly. Statistical analysis was performed using GraphPad Prism software. Unpaired parametric two tailed t-tests (with Welch's correction for unequal variance) were applied to determine P-values for the epithelial percentages shown in

the graph in Fig. 3E. The percentages of epithelial cells change significantly *in vivo* (P<0,0001) and *in silico* (P<0,0001).

Aspect ratio determination and ROC curve

The geometry of somites *in vivo* in controls and stretched embryos was described by measuring their length in rostro-caudal (x) and their width in medio-lateral (y) direction using the "Measure"-tool in ImageJ. Subsequently, the corresponding aspect ratio AR (AR = x/y) was calculated. Somites forming in controls and in stretched embryos after the second pull were measured upon their separation from the anterior tip of the PSM (Fig. S7A-B). Somites that had been formed before were measured at the end of the second pull (Fig. S7C). The aspect ratio of somites *in silico* was determined before (Fig. S7D) and after the application of the pull (Fig. S7E) accordingly (for strain regimes *in silico* see below). The corresponding receiver operating characteristics (ROC) curves (34–37) (Fig. 3H) were generated by performing a binary logistic regression using the Data Analysis Tool of the Real Statistics Excel plugin Realstats (available at http://www.real-statistics.com). We analyzed how well the aspect ratio of stretched somites *in vivo* and *in silico* can predict the binary outcome of whether a somite will undergo division or not. This is measured by the area under the curve (AUC) in the ROC diagram. The AUC can very between 0.5 (stochastic relation) and 1 (fully determined). 95% Confidence intervals for AUC values were calculated using the 'ROC curve analysis' tool of MedCalc software (available at https://www.medcalc.org/index.php).

Cellular Potts model of somite division

To understand the influence of mechanical stretching on somites and the somite division observed *in vivo*, we constructed a two-dimensional mathematical model based on the Cellular Potts Model (32, 55), representing a cross-section through a three-dimensional somitic tissue.

We made use of a compartmentalized Cellular Potts model (CPM), also known as Glazier-Graner-Hogeweg model. The model was implemented using CompuCell3D, an open source modeling package based on the CPM (33). CompuCell3D's 'compartmentalized cell' module implements the compartmental CPM that represents biological cells as a collection of sub-cellular domains, each identified by a unique cluster index. This module allows specification of separate contact energies between the domains of a single cell (internal parameters) as well as specification of external contact energy parameters between cells of the same type and of different types. For more information on CPM modeling or compartmentalized cell module, please refer to Swat *et al.* (33). Briefly, the compartmentalized CPM projects biological cells on a (usually regular, rectangular) lattice as domains of (usually) connected lattice sites. Each lattice site, $\vec{x}$, is associated with a domain index $\sigma(\vec{x})$ that identifies a biological cell, a cellular compartment, or a volume element of extracellular material. Cell identification number $\sigma = 0$ usually represents a generic 'medium'. Each domain σ has a type label $\tau\big(\sigma(\vec{x})\big) \in \mathbb{N}$ to represent the generic 'type' (subcellular domain, ECM, and so forth) and an additional label $\xi\big(\sigma(\vec{x})\big) \in \mathbb{N}$ that bundles compartments to a biological cell or connected extracellular material. Although each individual object (subcellular compartment, ECM medium etc.) has its own unique domain index σ, many objects may be associated with the same type label τ.

The evolution of our CPM is governed by a force-balance, represented by a Hamiltonian, H,

$$H = H_{contact} + H_{volume} + H_{spring} \ , \qquad (Eq. 1)$$

which describes the dynamics of cells (e.g. cell behaviors, properties and interactions). The Hamiltonian is minimized using a Metropolis algorithm that mimics microscopic membrane and material fluctuations, such that both the equilibrium and the transient towards the equilibrium can be physically and biologically interpreted (56). $H_{contact}$ represents the cell adhesion where cell-cell and cell-medium interactions take place through contact energies. The size of the interface between two cells defines the contact energy and is given by:

$$H_{contact} = \sum_{(\vec{x},\vec{x}')} J_{\tau(\sigma(\vec{x})),\tau\left(\sigma(\vec{x}')\right)} \left(1 - \delta_{\sigma(\vec{x}),\sigma(\vec{x}')}\right) \qquad (Eq. 2)$$

Here, $J_{\tau(\sigma(\vec{x})),\tau\left(\sigma(\vec{x}')\right)}$ is the bonding energy between two neighboring cell types $\tau(\sigma(\vec{x})$ and $\tau(\sigma(\vec{x}')$, and $\delta_{\sigma(\vec{x}),\sigma(\vec{x}')}$ is the Kronecker delta term in which adhesion is restricted to the cell membranes by eliminating the contributions from the neighboring lattice sites belonging to the same cell. If $\sigma(\vec{x}) = \sigma(\vec{x}')$, the delta function returns a value of 1 and 0 otherwise. The term H_{volume} in the Hamiltonian specified in Eq. 1 is given by:

$$H_{volume} = \sum_{\sigma} \lambda_{volume}\,(\sigma).[v(\sigma) - V(\sigma)]^2 \qquad (Eq. 3)$$

and constrains the cell volume, $v(\sigma)$, close to a resting volume $V(\sigma)$. The Lagrange multiplier λ_{volume} represents cell elasticity - higher values of λ_{volume} reduce fluctuations of cell's volume from its target volume.

Compartments of cells and subunits of the extracellular matrix can be mechanically coupled by connecting their centers of mass using springs. Each spring contributes an additional energy bias H_{spring} to the Hamiltonian in *Eq. S2*.

$$H_{spring} = \sum \lambda_{ij} \left(l_{ij} - L_{ij}\right)^2 \qquad (Eq. 4)$$

where l_{ij} is the absolute distance between the center of masses of cells i and j and L_{ij} is the specified target spring length. $\lambda_{ij}$is an elasticity parameter. Springs rupture if they exceed a threshold length; new springs are formed if cells move within a threshold distance. In our simulations, we have many cell types (epithelial internal compartments, extracellular matrix (ECM), and epithelial cell (apical)) which are connected using springs. Details on these cell-specific spring lengths and elasticity are explained in the next sections of the supplementary material.

The CPM is updated using a Metropolis algorithm, which mimics the extension and retraction of pseudopods of the biological cells, and fluctuations of the extracellular matrix materials. The algorithm iteratively selects a lattice site $\vec{x}$ and attempts to copy its cell index $\sigma(\vec{x})$ into a randomly chosen adjacent lattice site $\vec{x}'$. This is called a copy attempt. The probability of accepting or rejecting the attempted copy update is based on the energy minimization criteria and follows Boltzmann probability,

$$P\ (\sigma(\vec{x})\ \rightarrow\ \vec{x}') = \begin{cases} 1 & ,\Delta H\ (\sigma(\vec{x})\ \rightarrow\ \vec{x}') < 0 \\ e^{\frac{-\Delta H(\sigma(\vec{x}) \rightarrow \vec{x}')}{T}} & ,\Delta H\ (\sigma(\vec{x})\ \rightarrow\ \vec{x}') \geq 0 \end{cases} \qquad (Eq. 5)$$

where $\Delta H(\sigma(\vec{x}) \rightarrow \vec{x}')$ represents the change in the Hamiltonian due to the copy attempt. *Eq. 5* shows that if the attempted copy update will reduce the energy, i.e. $\Delta H(\sigma(\vec{x}) \rightarrow \vec{x}') < 0$, the update is accepted with a probability of 1. However, if the energy increases due to the copy-attempt, the system follows Boltzmann probability to accept or reject a copy-attempt. The parameter T is the cellular temperature, representing the amplitude of active cell membrane fluctuations or fluctuations of the extracellular materials.

The model included the following assumptions: (i) the tissue surrounding the somite can be approximated as elastic, and was modeled as a non-specified extracellular matrix (ECM); (ii) the somite consists of polarized epithelial cells forming the outer layer (18), while the somite core (somitocoel) consists of unpolarized mesenchymal cells. The mesenchymal cells in the core of the somite were represented by single-compartment, non-coupled and non-polarized cells. Following Dias *et al.* (18) the epithelial cells in our model consisted of three domains, called 'apical', and 'lateral' and 'basal' (Fig. S9). The three compartments were initially distributed at random inside an epithelial cell and after a brief relaxation period of 1500 MCS (epithelial polarization time), these compartments were connected internally to one another using linear elastic springs (Eq. 4). To achieve epithelial elongation (Fig. S9), target lengths of all internal springs ($L_{apical-lateral}$, $L_{apical-basal}$, $L_{lateral-basal}$) were individually incremented by 1 every 20th MCS within the elongation time frame (1500 MCS), until every spring reached its final specified target length ($L_{apical-lateral} = 15, L_{apical-basal} = 30,\ L_{lateral-basal} = 20$). The ECM, with its main functional component fibronectin *in vivo* (57), was modeled as a network of cells. These ECM cells were also connected to each other using elastic springs of target length $L_{ecm-ecm} = 10$ with elastic stiffness $\lambda_{ecm-ecm} = 200$. This was necessary to obtain a desired stiffness of the ECM in order to keep it intact during and after stretching.

We first attempted to construct a well-organized, initial epithelial structure as a starting point for the stretching model. Contact energies between domains as well as contact energies with other cell types and the ECM were set according to S3 Table. In absence of quantitative values for the adhesion strengths and interfacial tensions between the cells, we estimated parameter values for which a stable epithelial monolayer is maintained in our simulations, followed by parameter sensitivity studies. We assumed the apical domains of adjacent epithelial cohered strongly, following Dias *et al.*'s (18) assumption mimicking the distribution of N-Cadherin *in vivo* (58). The lateral domains of epithelial cells (between the apical and basal domains) adhere strongly to each other, similar to Cadherin mediated cohesion *in vivo* (25, 26). To represent the apical actin ring, each center of mass of an apical unit was connected to the center of mass of neighboring apical domains on either side (left and right) using elastic springs of a resting length of $L_{ij} = 4$ with elastic stiffness $\lambda_{apical-apical} = 100$.

The monolayer of epithelial cells was constructed by initializing the simulation with a collection of mesenchymal cells surrounded by an elastic ECM. We selected a mesenchymal cell at the boundary with the surrounding ECM and made it epithelial. This first epithelialized cell induced MET in neighboring cells based on basolateral contact (41, 42), which finally led to a fully epithelialized somite-like structure (initial phase of Movie S3).

After a stable, somite-like, epithelial structure had formed, we gradually strained the extracellular matrix in our simulations, in order to mimic the experimental setup. To this end, we connected two 'walls' constructed out of immobile cells to the left and right-hand ends of the ECM using stiff elastic springs and slowly moved the walls apart by 1 pixel every 50 MCS, using a technique introduced previously for simulating the compression of tissue spheroids (59) and the application of stents in arteries (60)

The stretching rate was sufficiently slow (walls moved outward by 1 pixel every 50 MCS), such that it did not damage the ECM cells (Phase 2 in Movie S3). We tested three MET scenarios for their ability to allow the stretched somite to divide into epithelialized daughter somites. We first assumed that somites can divide by reorganization of existing epithelial cells and allowed no MET after the stretching. We could successfully deform the somite by stretching, but neither small nor large strains induced somite division (Fig. S10, top row). This suggested the necessity of an MET mechanism to enable somite division. In the second scenario, a mesenchymal cell underwent MET after contact with the surrounding ECM for a certain time (600 MCS). We did not observe somite division for different levels of deformation, probably because intercellular connections between epithelial cells did not soften completely upon stretching, thereby avoiding sufficient contact between mesenchymal somitocoel cells and the surrounding ECM to induce additional MET (Fig. S10, middle row). In the third scenario, the MET occurred after sufficiently long contact of mesenchymal cells to the basal or lateral membrane of epithelial cells (600 MCS). Upon stretching, several springs between neighboring apical compartments released and mesenchymal cells from the core became exposed to the lateral or basal membranes of epithelial cells leading to additional MET. These additional epithelial cells disturbed the equilibrium and could not get incorporated into the original epithelial ring. So, the epithelium started to reorganize and divide into daughter somites (Fig. S10, bottom row and Phase 3 in Movie S3).

Based on our observations that daughter somites are separated and presumably stabilized by a newly forming fibronectin matrix (Fig. S4), we also implemented a similar rule for ECM production by the basal units of epithelial cells. If the basal domain of an epithelial cells is not attached to a specified amount of ECM (given by threshold value) for a certain duration, it produces an additional ECM cell. This production continues until the threshold value is reached again. Such

production of the fibronectin allows the dividing somites to separate from each other permanently. The parameters used in the simulations are shown in the S3 Table. For a systematical analysis of how well the geometry of stretched somite predicts division we applied lateral wall displacements of 30 to 110 pixels (15 to 55 pixels per side), resulting into aspect ratio values similar to stretched somites *in vivo* (Fig. 3G).

The *in silico* somite model can be parameterized to the experimentally observed ratio of mesenchymal and epithelial cells**.** Fig. S11 shows that, following the MET based on the basolateral contact rule, initial epithelialization of the somite and division of the somites after stretching can be achieved with a large core and small core somite.

In order to further validate the *in silico* model, we also tested the influence of decreased cohesion between lateral domains of epithelial cells in epithelializing, non-stretched somites. Similar to results in *N-Cadherin/cad11* double-homozygous mouse mutants (25), we observed subdivisions into small cell clusters of epithelioid morphology (Fig. S12).

ACKNOWLEDGEMENTS

We are grateful to Julio Belmonte for his advice on the simulations at the early stages of model development. We thank Stuart A. Newman and Frietson Galis for valuable comments during the final preparation of the manuscript.

FUNDING DISCLOSURE

Parts of this research were funded by ZonMW VICI grant 918.11.635 and by NWO VIDI grant 864.10.009.

AUTHOR CONTRIBUTIONS

B.N. and M.S. performed the experiments and analyzed the data. H.T. and R.M. performed the simulations. T.S. and R.M. supervised the project. All authors wrote the manuscript.

REFERENCES

1. Richardson MK, Allen SP, Wright GM, Raynaud a, Hanken J (1998) Somite number and vertebrate evolution. *Development* 125:151–160.
2. Galis F, et al. (2014) Fast running restricts evolutionary change of the vertebral column in mammals. *Proc Natl Acad Sci* 111(31):11401–11406.
3. Kulesa PM, Schnell S, Rudloff S, Baker RE, Maini PK (2007) From segment to somite: Segmentation to epithelialization analyzed within quantitative frameworks. *Dev Dyn* 236(May):1392–1402.
4. Martins GG, et al. (2009) Dynamic 3D cell rearrangements guided by a fibronectin matrix underlie somitogenesis. *PLoS One* 4(10):e7429.
5. Hubaud A, Pourquié O (2014) Signalling dynamics in vertebrate segmentation. *Nat Rev Mol Cell Biol* 15(11):709–721.
6. Gomez C, et al. (2008) Control of segment number in vertebrate embryos. *Nature* 454(7202):335–339.
7. Hubbs CL (1922) Variations in the Number of Vertebrae and Other Meristic Characters of Fishes Correlated with the Temperature of Water during Development. *Am Nat* 56(645):360.
8. Beacham TD, Murray CB (1986) The Effect of Spawning Time and Incubation Temperature on Meristic Variation in Chum Salmon Oncorhynchus-Keta. *Can J Zool* 64(1):45–48.
9. Tibblin P, Berggren H, Nordahl O, Larsson P, Forsman A (2016) Causes and consequences of intra-specific variation in vertebral number. *Sci Rep* 6(April):26372.
10. Jockusch EL (1997) Geographic variation and phenotypic plasticity of number of trunk vertebrae in Slender Salamanders, Batrachoseps (Caudata: Plethodontidae). *Evolution (N Y)* 51(6):1966–1982.
11. Peabody RB, Brodie Jr. ED (1975) Effect of Temperature, Salinity and Photoperiod on the

Number of Trunk Vertebrae in Ambystoma maculatum. *Copeia* 1975(4):741–746.

12. Osgood DW (1978) Effects of temperature on the development of meristic characters in Natrix fasciata. *Copeia* 1978(1):33–47.
13. Lecyk M (1966) The effect of hyperthermia applied in the given stages of pregnancy on the number and form of vertebrae in the offspring of white mice. *Experientia* 22(4):254–255.
14. Lindsey CC, Moodie GEE (1967) THE EFFECT OF INCUBATION TEMPERATURE ON VERTEBRAL COUNT IN THE CHICKEN. *Can J Zool* 45(5):891–892.
15. Alberch P (1992) Nitecki, M. H. (ed.) Evolutionary Innovations. The University of Chicago Press (1990) ISBN: 0-226-58695-2. *J Evol Biol* 5(4):717–719.
16. Laland KN, et al. (2015) The extended evolutionary synthesis: its structure, assumptions and predictions. *Proc R Soc B Biol Sci* 282(1813):20151019.
17. Müller GB (2003) Embryonic motility: Environmental influences and evolutionary innovation. *Evol Dev* 5(1):56–60.
18. Dias AS, de Almeida I, Belmonte JM, Glazier JA, Stern CD (2014) Somites Without a Clock. *Science (80-)* 343(6172):791–795.
19. Tam PP (1981) The control of somitogenesis in mouse embryos. *J Embryol Exp Morphol* 65 Suppl:103–128.
20. Stern CD, Bellairs R (1984) The roles of node regression and elongation of the area pellucida in the formation of somites in avian embryos. *J Embryol Exp Morphol* 81:75–92.
21. Duess JW, Fujiwara N, Corcionivoschi N, Puri P, Thompson J (2013) ROCK inhibitor (Y-27632) disrupts somitogenesis in chick embryos. *Pediatr Surg Int* 29(1):13–8.
22. Hubaud A, Regev I, Mahadevan L, Pourquié O (2017) Excitable Dynamics and Yap-Dependent Mechanical Cues Drive the Segmentation Clock. *Cell*. doi:10.1016/j.cell.2017.08.043.

23. Hamburger V, Hamilton HL (1951) A series of normal stages in the development of the chick embryo. *J Morphol* 88(1):49–92.

24. Schmitz M, Nelemans BKA, Smit TH (2016) A Submerged Filter Paper Sandwich for Long-term Ex Ovo Time-lapse Imaging of Early Chick Embryos. (118):e54636.

25. Horikawa K, Radice G, Takeichi M, Chisaka O (1999) Adhesive Subdivisions Intrinsic to the Epithelial Somites. *Situ* 215:182–189.

26. Kimura Y, et al. (1995) Cadherin-11 expressed in association with mesenchymal morphogenesis in the head, somite, and limb bud of early mouse embryos. *Dev Biol* 169:347–358.

27. Watanabe T, Sato Y, Saito D, Tadokoro R, Takahashi Y (2009) EphrinB2 coordinates the formation of a morphological boundary and cell epithelialization during somite segmentation. *Proc Natl Acad Sci U S A* 106(18):7467–72.

28. Barrios A, et al. (2003) Eph / Ephrin Signaling Regulates the Mesenchymal- to-Epithelial Transition of the Paraxial Mesoderm during Somite Morphogenesis. *Curr Biol* 13:1571–1582.

29. Morimoto M, et al. (2007) The negative regulation of Mesp2 by mouse Ripply2 is required to establish the rostro-caudal patterning within a somite. *Development* 134(8):1561–9.

30. Schrägle J, Huang R, Christ B, Pröls F (2004) Control of the temporal and spatial Uncx4.1 expression in the paraxial mesoderm of avian embryos. *Anat Embryol (Berl)* 208(4):323–32.

31. Christ B, Ordahl CP (1995) Early stages of chick somite development. *Anat Embryol (Berl)* 191(5):381–396.

32. Glazier, Graner (1993) Simulation of the differential adhesion driven rearrangement of biological cells. *Phys Rev E Stat Phys Plasmas Fluids Relat Interdiscip Topics* 47(3):2128–

2154.

33. Swat MH, et al. (2012) Multi-Scale Modeling of Tissues Using CompuCell3D. *Methods Cell Biol* 110:325–366.

34. Lusted LB (1971) Decision-making studies in patient management. *N Engl J Med* 284(8):416–424.

35. Goodenough DJ, Rossmann K, Lusted LB (1974) Radiographic applications of receiver operating characteristic (ROC) curves. *Radiology* 110(1):89–95.

36. Metz CE (1978) Basic principles of ROC analysis. *Semin Nucl Med* 8(4):283–298.

37. Hanley AJ, McNeil JB (1982) The Meaning and Use of the Area under a Receiver Operating Characteristic (ROC) Curve. *Radiology* 143:29–36.

38. Nagai H, Sezaki M, Nakamura H, Sheng G (2014) Extending the limits of avian embryo culture with the modified Cornish pasty and whole-embryo transplantation methods. *Methods* 66(3):441–446.

39. Dubrulle J, Pourquié O (2004) fgf8 mRNA decay establishes a gradient that couples axial elongation to patterning in the vertebrate embryo. *Nature* 427(6973):419–22.

40. Jackson TR, Kim HY, Balakrishnan UL, Stuckenholz C, Davidson LA (2017) Spatiotemporally Controlled Mechanical Cues Drive Progenitor Mesenchymal-to-Epithelial Transition Enabling Proper Heart Formation and Function. *Curr Biol* 27(9):1326–1335.

41. Baum B, Georgiou M (2011) Dynamics of adherens junctions in epithelial establishment, maintenance, and remodeling. *J Cell Biol* 192(6):907–917.

42. Campbell K, Casanova J, Skaer H Mesenchymal-to-epithelial transition of intercalating cells in Drosophila renal tubules depends on polarity cues from epithelial neighbours. *Mech Dev* 127(7–8):345–57.

43. Braendle C, Flatt T (2006) A role for genetic accommodation in evolution? *BioEssays*

28(9):868–873.

44. Fusco G, Minelli A (2010) Phenotypic plasticity in development and evolution: facts and concepts. *Philos Trans R Soc B Biol Sci* 365(1540):547–556.

45. Lopez TP, Fan C-M (2013) Dynamic CREB family activity drives segmentation and posterior polarity specification in mammalian somitogenesis. *Proc Natl Acad Sci U S A* 110(22):E2019-27.

46. Galis F, et al. (2014) Fast running restricts evolutionary change of the vertebral column in mammals. *Proc Natl Acad Sci* 111(31):11401–11406.

47. Slijepčević M, Galis F, Arntzen JW, Ivanović A (2015) Homeotic transformations and number changes in the vertebral column of Triturus newts. *PeerJ* 3(11):e1397.

48. Carapuço M, Nóvoa A, Bobola N, Mallo M (2005) Hox genes specify vertebral types in the presomitic mesoderm. *Genes Dev* 19(18):2116–2121.

49. Dubrulle J, McGrew MJ, Pourquié O (2001) FGF signaling controls somite boundary position and regulates segmentation clock control of spatiotemporal Hox gene activation. *Cell* 106(2):219–232.

50. Mallo M, Wellik DM, Deschamps J (2010) Hox genes and regional patterning of the vertebrate body plan. *Dev Biol* 344(1):7–15.

51. Kaliontzopoulou A, Llorente G, Carretero M (2008) Interspecific and intersexual variation in presacral vertebrae number in Podarcis bocagei and P. carbonelli. *Amphibia-Reptilia* 29(2):288–292.

52. Chapman SC, Collignon J, Schoenwolf GC, Lumsden A (2001) Improved method for chick whole-embryo culture using a filter paper carrier. *Dev Dyn* 220(3):284–289.

53. Pannett C, Compton A (1924) the Cultivation of Tissues in Saline Embryonic Juice. *Lancet* 203(5243):381–384.

54. Voiculescu O, Papanayotou C, Stern CD (2008) Spatially and temporally controlled electroporation of early chick embryos. *Nat Protoc* 3(3):419–426.

55. Graner F, Glazier JA (1992) Simulation of Biological Cell Sorting Using a 2-Dimensional Extended Potts-Model. *Phys Rev Lett* 69(13):2013–2016.

56. Newman MEJ, Barkema GT (1999) *Monte Carlo Methods in Statistical Physics* (Clarendon Press Oxford).

57. P.Rifes, thesis: Fibronectin cues during somite formation, Universidade de Lisboa (2013).

58. Chal J, Guillot C, Pourquié O (2016) PAPC couples the Segmentation Clock to somite morphogenesis by regulating N-cadherin dependent adhesion. *bioRxiv*. doi:10.1101/071084.

59. Marmottant P, et al. (2009) The role of fluctuations and stress on the effective viscosity of cell aggregates. *Proc Natl Acad Sci U S A* 106(41):17271–17275.

60. Tahir H, Niculescu I, Bona-Casas C, Merks RMH, Hoekstra AG (2015) An in silico study on the role of smooth muscle cell migration in neointimal formation after coronary stenting. *J R Soc Interface* 12(108).

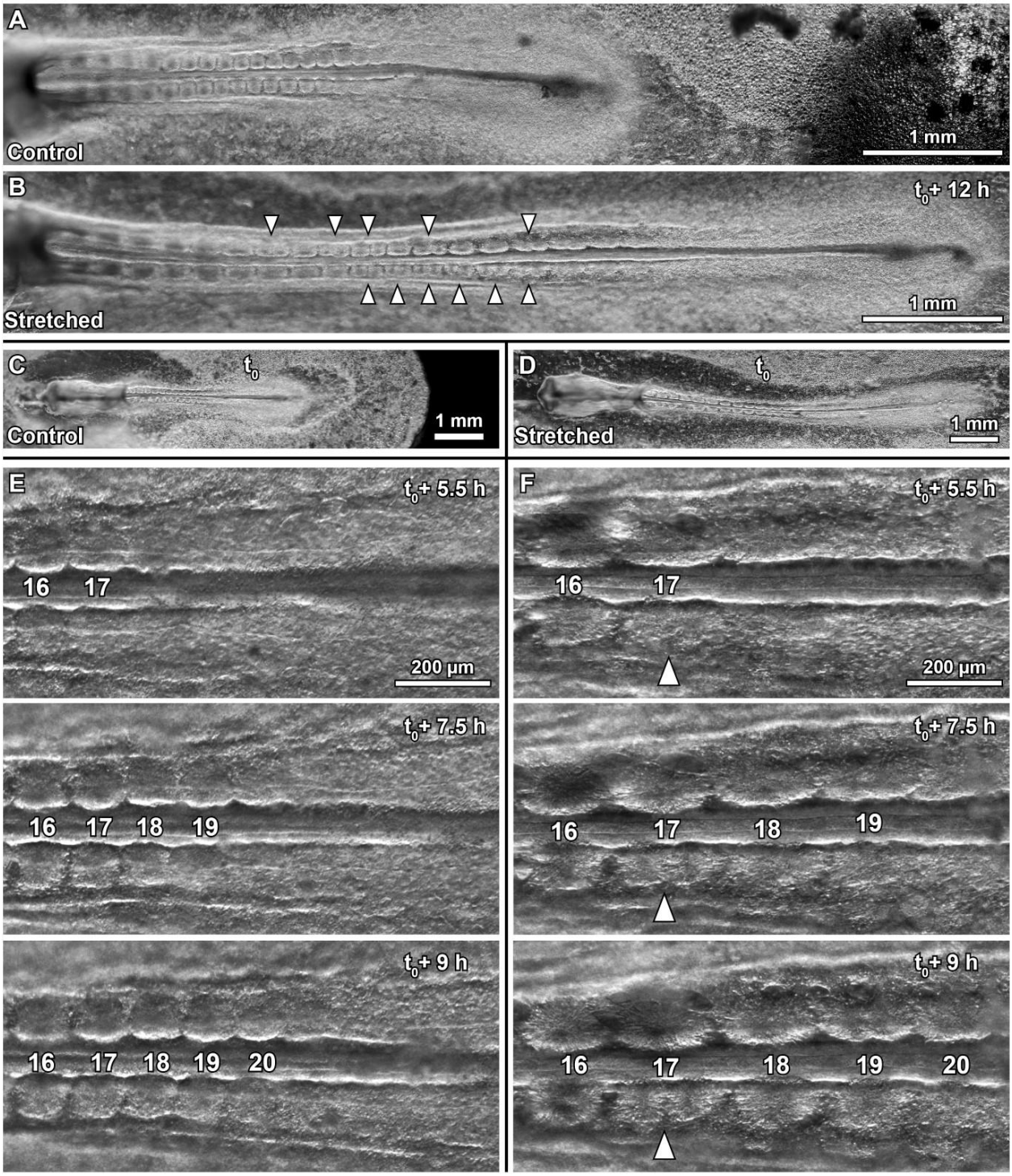

Fig. 1: Daughter somite formation in stretched chicken embryos.

Dark-field microscopy images of age-matched (**A**) control and (**B**) stretched embryo. Anterior is to the left in all images, arrowheads indicate divided somites, t_0 = end of stretch protocol, ventral

view. Difference in axial length becomes obvious between control embryo (**C**) and stretched embryo (**D**) (t_0: both embryos are at the 13-somite stage). Selected time-lapse frames of the segmenting PSM in control embryo (**E**) and stretched embryo (**F**). White arrowhead indicates daughter somite formation.

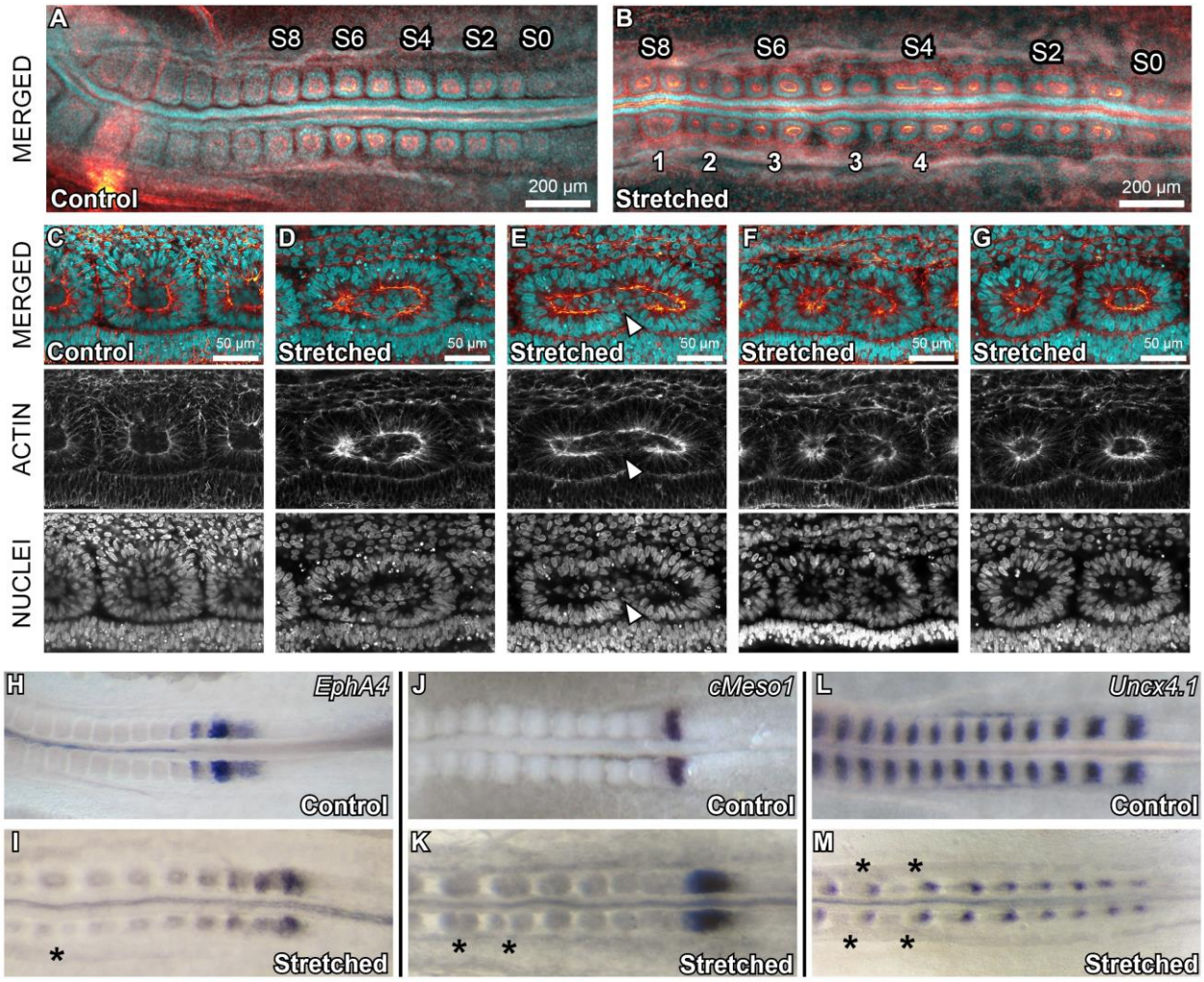

Fig. 2: Immunohistochemistry and in situ hybridizations of stretched and control embryos. Control (**A**) and stretched embryo (**B**), anterior is left, somite numbers are indicated (31). Scale bars, 200 µm. (B) Daughter somites can form unilaterally (1), equally (4) or unequally sized (3) and subdivide further (2). (**C**-**G**) Confocal cross-sections of selected somites of the same control (**C**) and stretched embryo (**D**-**G**). Anterior is left and medial below. Panels are arranged in potential order to illustrate the transition from a mechanically deformed somite (**D**) to two daughter somites (**G**). Cells from the somitocoel seem to gain an elongated morphology, possibly before incorporation into the epithelium (arrowhead in **E**). (**H**-**M**) In situ hybridizations for EphA4,

cMeso1 and Uncx4.1 show that EphA4 expression is induced around the somitocoels (**I**), while no new rostro-caudal polarity is induced in the daughter somites (indicated by *).

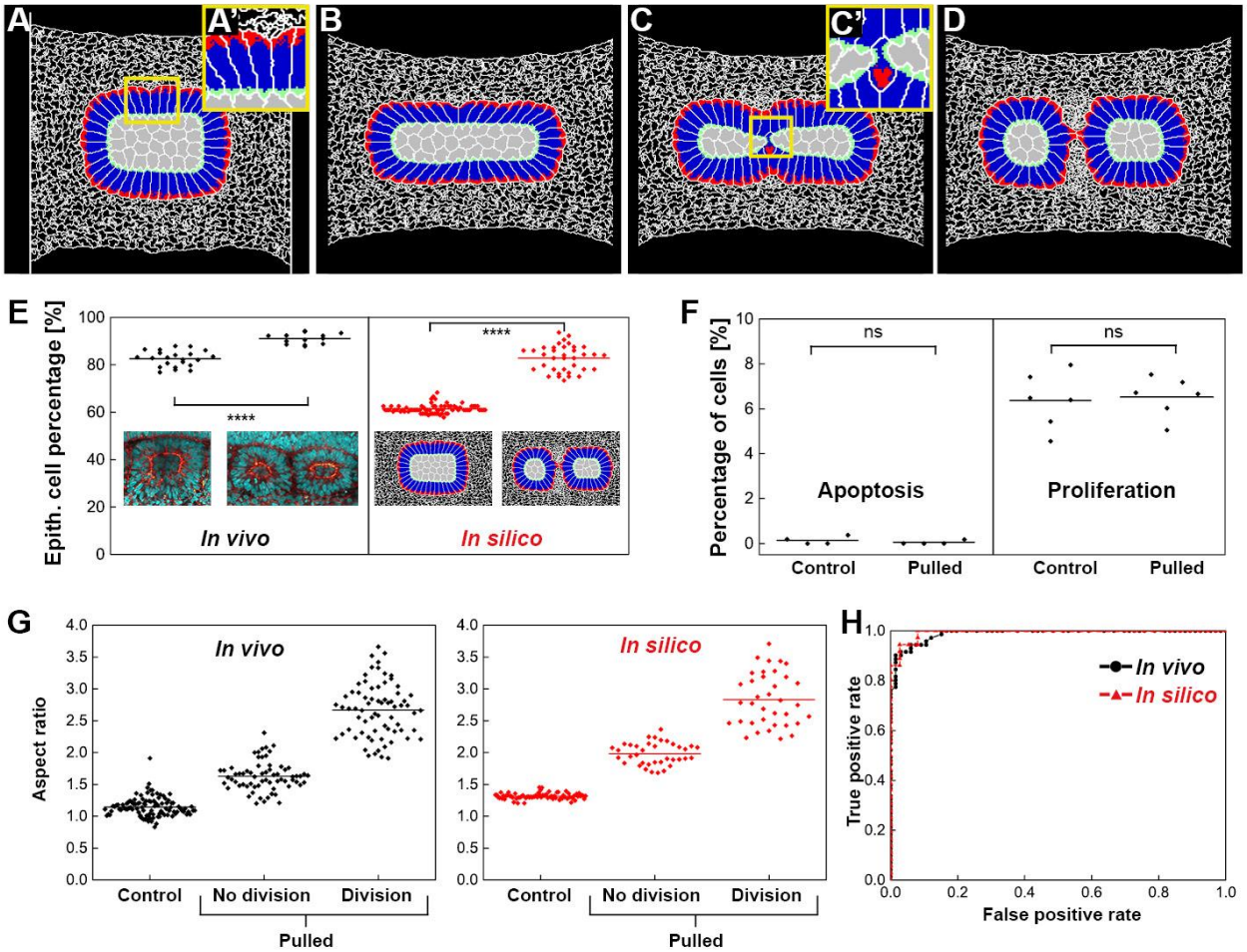

Fig. 3: Cellular Potts model of somite remodeling in comparison to daughter somite formation *in vivo*. (**A-D**) Daughter somite formation *in silico*, induced by stretching. Mesenchymal cells (grey) and extracellular matrix (white mesh), (**A'**) epithelial cells consisting of apical (green), lateral (blue) and basal (red) domains. (**C'**) Somitocoel cells undergoing MET. (**E**) Percentages of epithelial cells in control and divided somites *in silico* and *in vivo*, average line is shown. Significant increase of epithelial cell fraction *in vivo* (P<0.0001) and *in silico* (P<0.0001). (**F**) Apoptotic and proliferation rates in somitic mesoderm of control and stretched embryos. Differences non-significant (Mann-Whitney test, apoptosis P=0.43, proliferation P=0.79). (**G**) Somite aspect ratios *in vivo* and *in silico*. Point clouds and average lines are given. (H) ROC curves

for daughter somite formation *in vivo* and *in silico*, in dependence of aspect ratio of deformed somites. AUC is *0.989* (*in vivo*, 95% CI: 0.953-0.999) and 0.993 (*in silico*, 95% CI: 0.938-1.000).

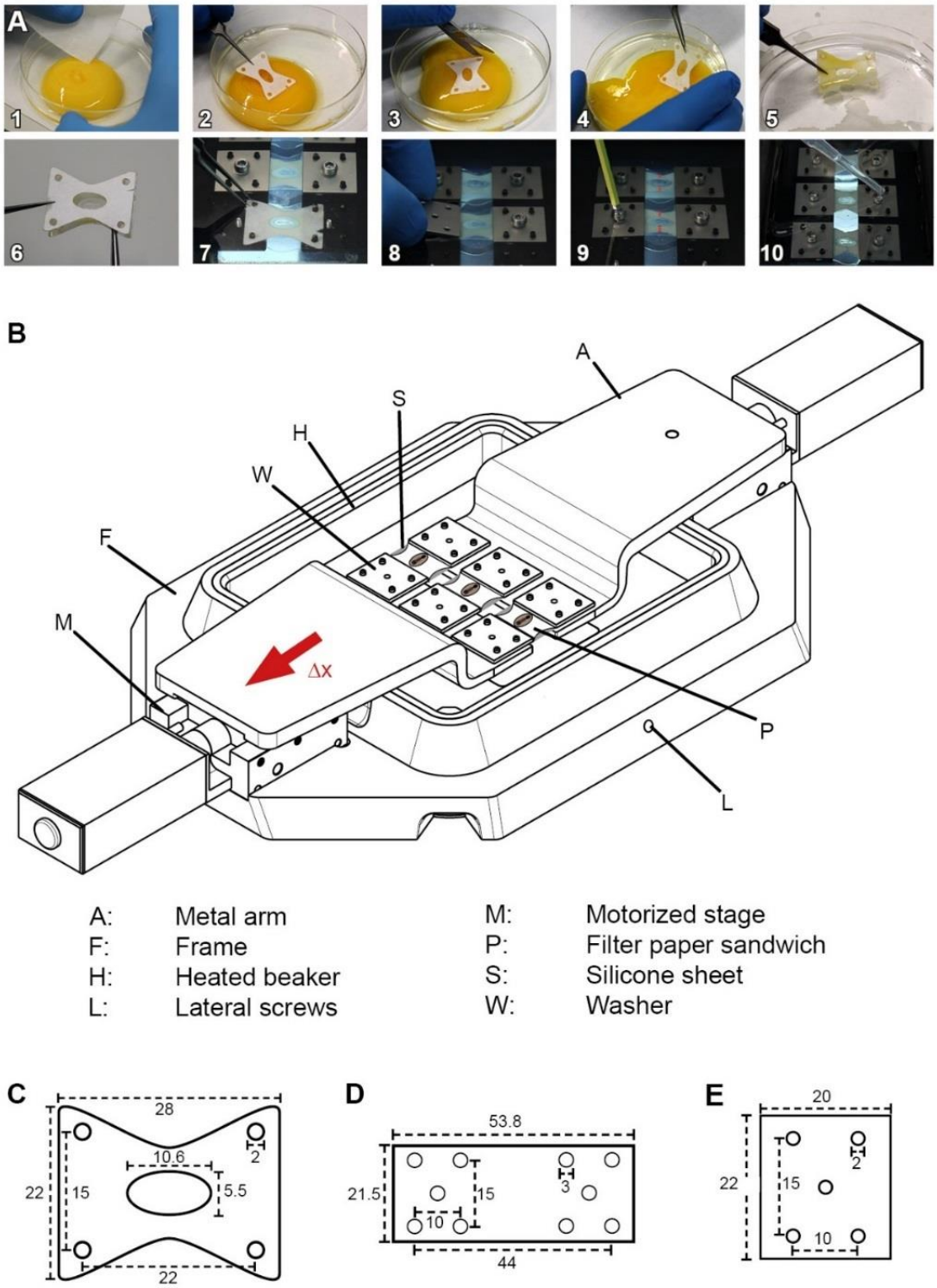

Fig. S1: Chick embryo stretching *ex ovo,* experimental setup. (A) Explantation procedure (24). (1) An egg is cracked into petri-dish and thick albumen removed from top of the yolk. (2) A filter

paper carrier is placed on top of the yolk, surrounding the blastoderm. (3) The filter paper carrier is cut loose from the surrounding vitelline membrane and (4) removed from top of the yolk. (5) Remaining yolk is carefully washed away in a saline bath. (6) The embryo is sandwiched with a second filter paper carrier. (7) The filter paper sandwich is submerged into the medium and hooked into the pins of the motorized arms. A thin sheet of PDMS protects the embryo from convection of the medium. (8) Washer plates clamp the filter paper sandwich to the metal arms and (9) are carefully pressed down by nuts. Filter paper sandwiches are cut along dashed red lines for later stretching of embryos. (10) The medium is covered with a layer of light mineral oil. (B) Schematic view of the embryo stretcher. The frame carries the motorized stages and keeps the temperature-controlled medium container in position. The whole setup is placed on a motorized x-y-stage, embryos are imaged from above and illuminated from below through the glass bottom of the medium container. (C) Filter paper carrier dimensions (in mm). (D) Dimensions of stencil for PDMS sheets (in mm). (E) Dimensions of metal washers used to clamp the filter paper (in mm).

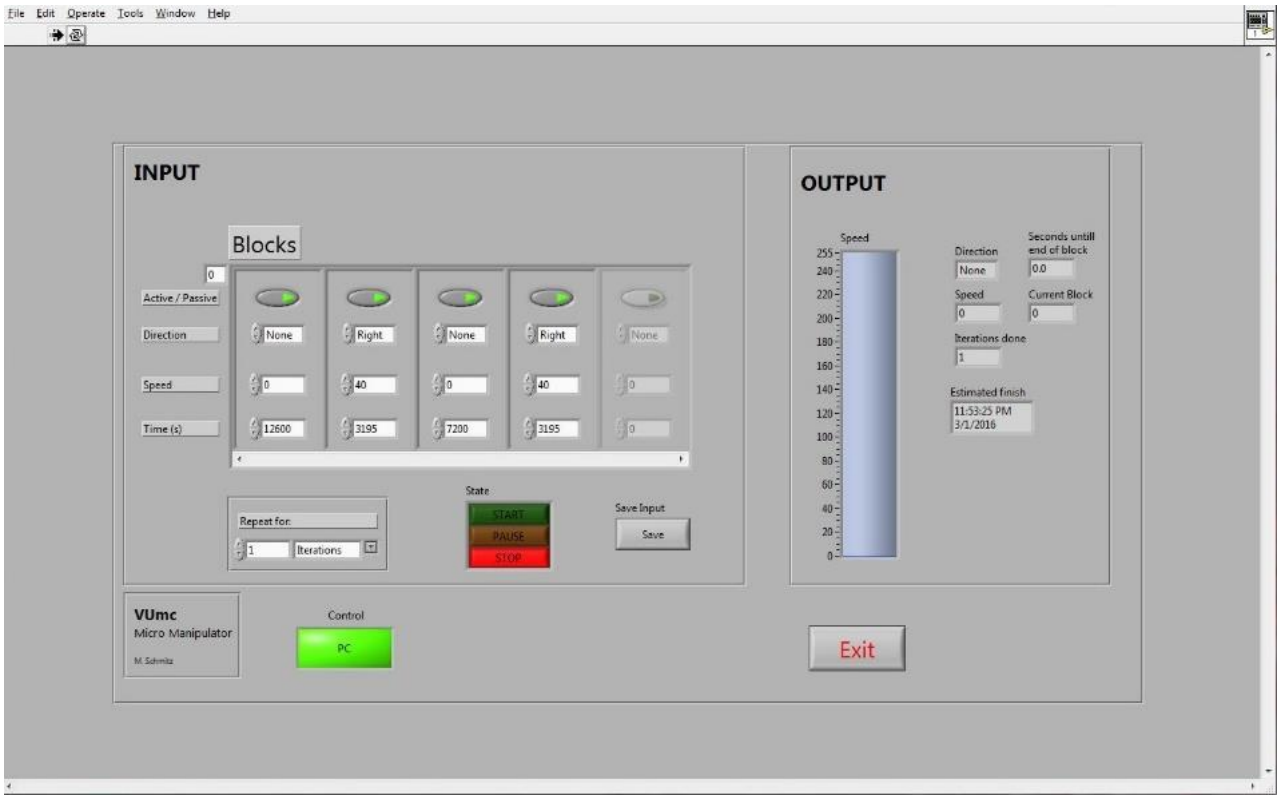

Fig. S2: User interface of the custom-made LabVIEW routine used to control one motorized translation stage of the embryo stretcher. Four experimental blocks are activated, defining the resting time after covering the culture medium with light mineral oil (12600 s/3.5 hrs), the first pulling block (3195 s), a resting time in between pulls (7200 s/2 hrs) and the second pulling block (3195 s).

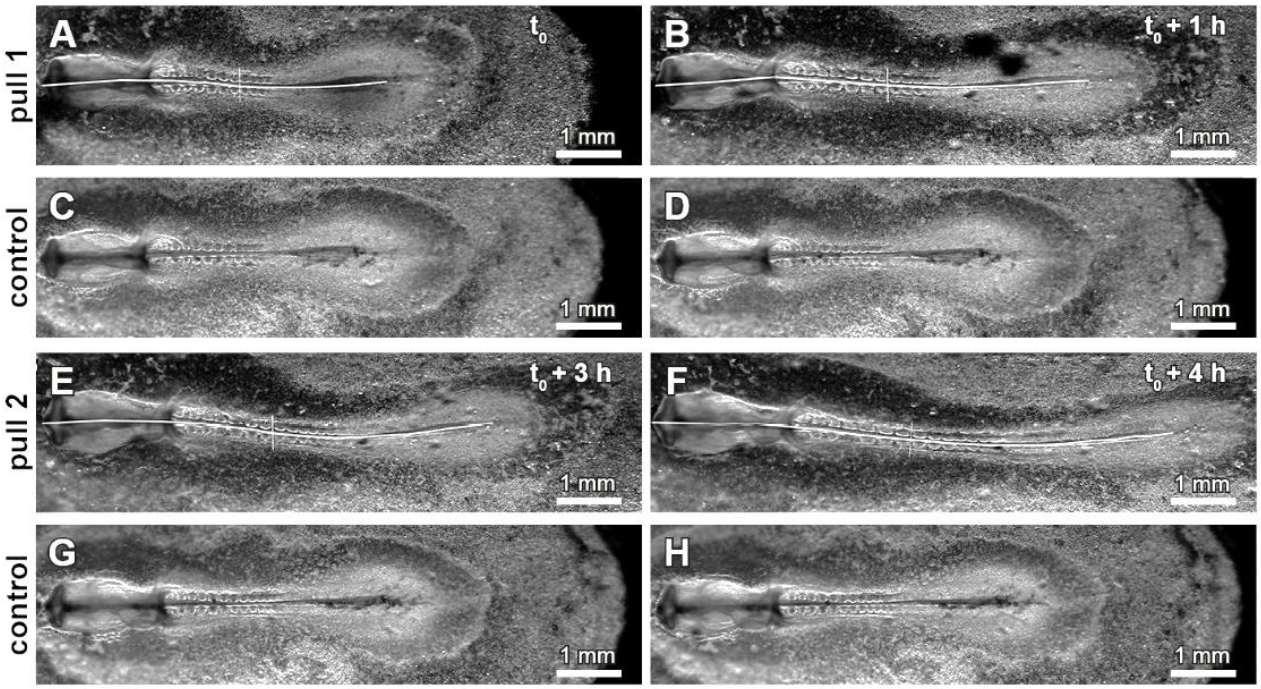

Fig. S3: Macroscopic deformation of pulled embryos. Before application of the first pull, experimental embryo (A) and control (C) are similar in axial length. The first pull increases the axial length of the pulled embryo considerably compared to the control (compare B and D). This length difference remains over the waiting period between first and second pull (compare B and D and E and G). The second pull increases the length difference between pulled embryo and control even further (compare F and H).

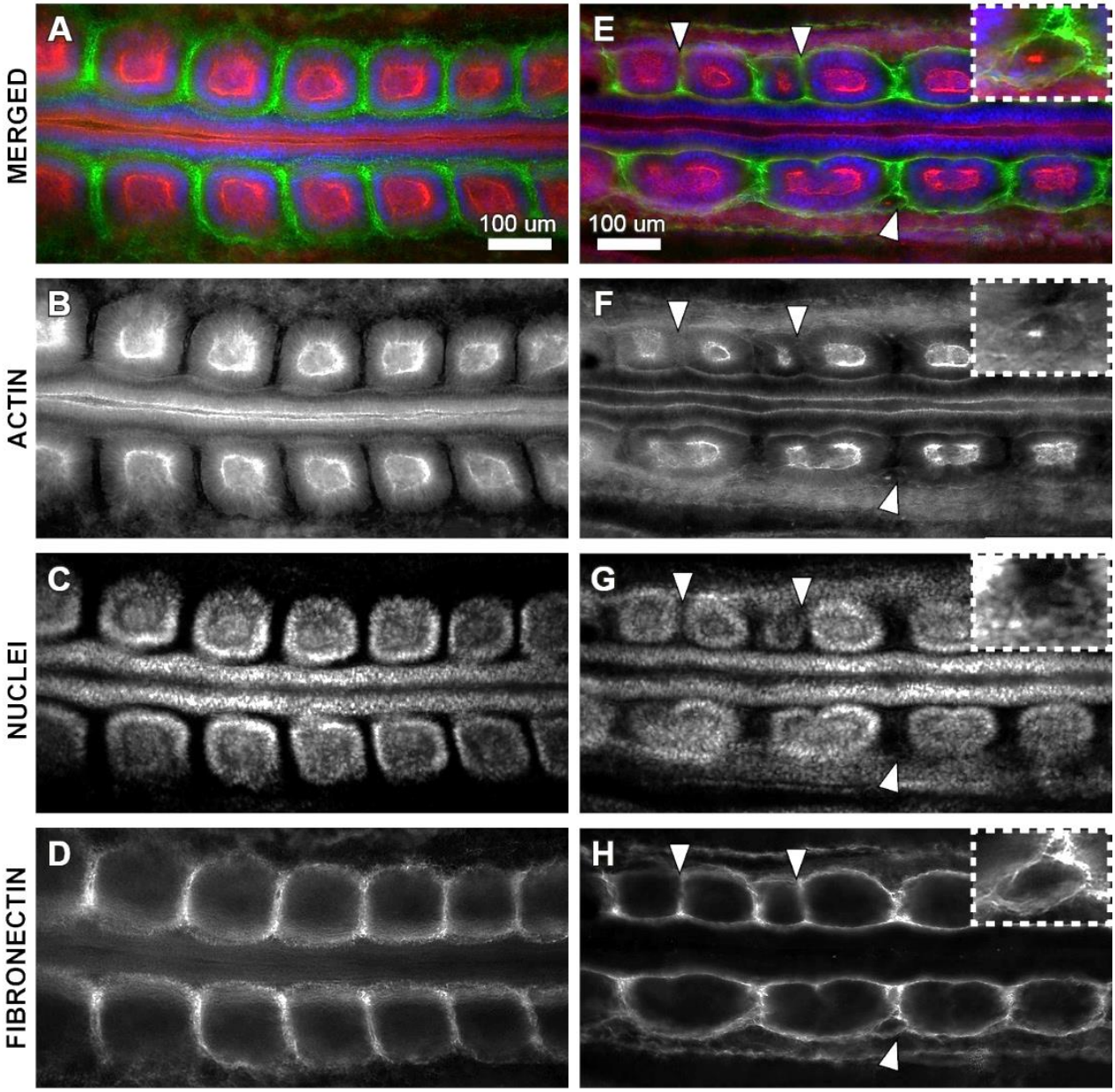

Fig. S4: Fibronectin distribution around daughter somites. Widefield fluorescent micrographs of control embryo (A-D) and stretched embryo (E-H) stained for actin (red), DNA in cell nuclei (blue) and extracellular matrix component fibronectin (green). Ventral view, anterior is to the left. Daughter somites are surrounded and separated from each other by a newly formed fibronectin matrix (white arrowheads in E and H) and can be extremely small (inset E to H) and lacking a mesenchymal core.

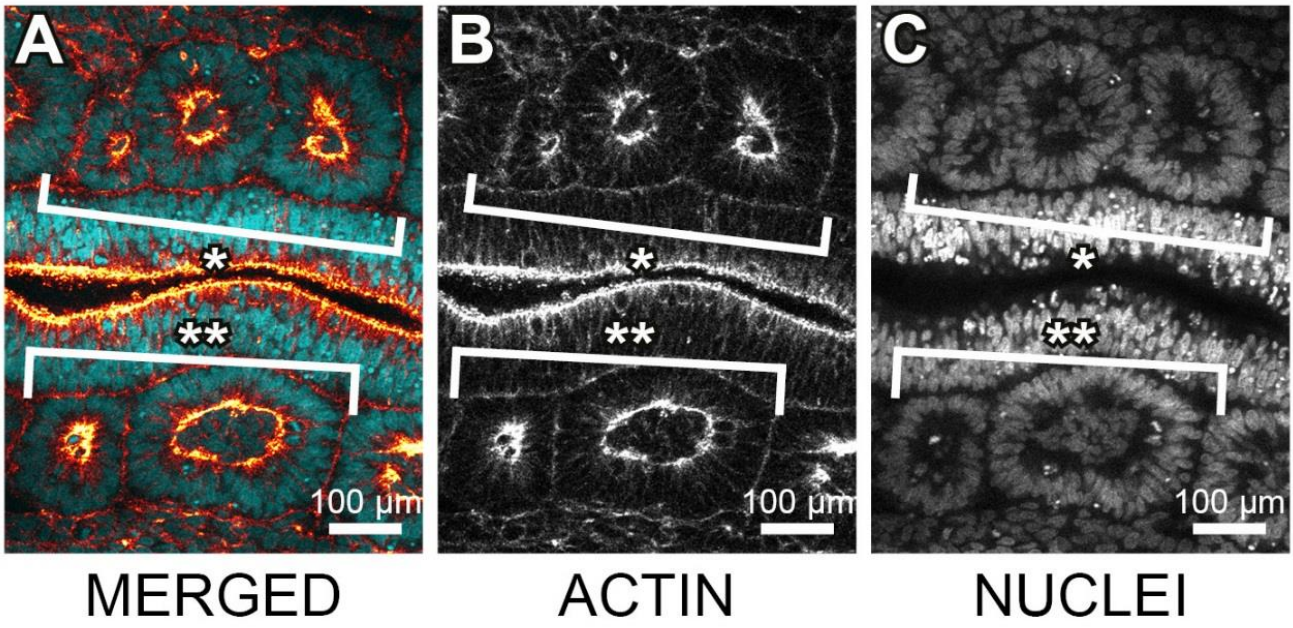

Fig. S5: Versatile daughter somite morphologies. Confocal micrograph of daughter somites on both sides of the midline in stretched and fixated chick embryo stained for actin (red) and DNA in cell nuclei (blue). Anterior is to the left, ventral view. Daughter somites do not only result from splitting into anterior and posterior compartment of original somite, but can also reorganize into three daughter somites (*) or two unequally sized daughter somites (**).

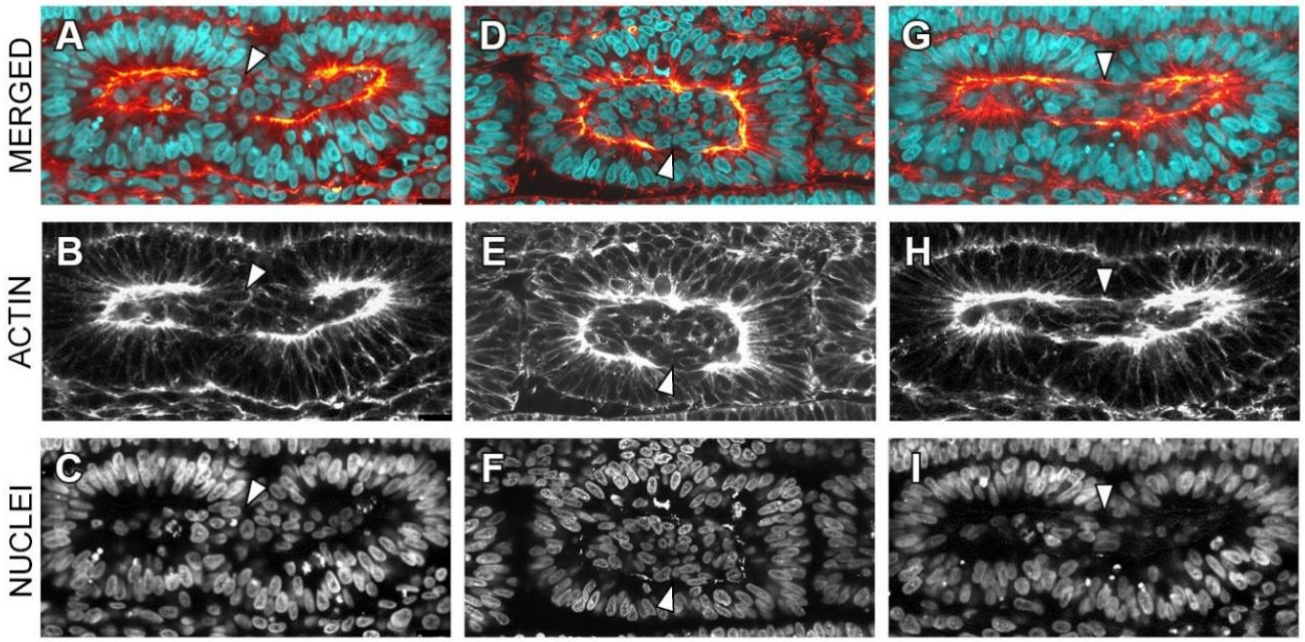

Fig. S6: Fracture of epithelial sheet and potential MET of mesenchymal somitocoel cells. Confocal micrograph of somites, fixated during daughter somite formation in stretched chick embryos, stained for actin (orange) and DNA in cell nuclei (cyan). Anterior is to the left. White arrowheads indicate discontinuities in the apical actin ring of the somitic epithelium, suggesting a local opening of the epithelial sheet and potential interfaces for the recruitment of additional mesenchymal cells from the somitocoel for their incorporation into the existing epithelium.

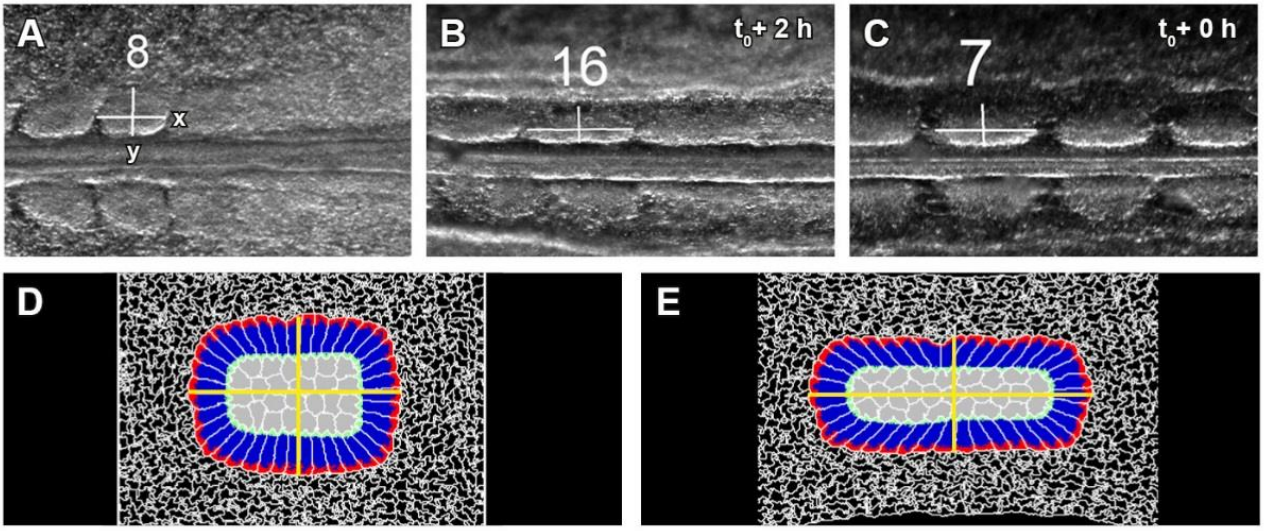

Fig. S7: Determination of somite aspect ratios. Measuring the length (x) and width (y) of somites upon separation from the anterior tip of the PSM in control embryos (A) and stretched embryos (B), and after application of the second pull (C). Somites in (B) and (C) underwent division later. Anterior is to the left. Aspect ratio determination *in silico* before (D) and after (E) the pull.

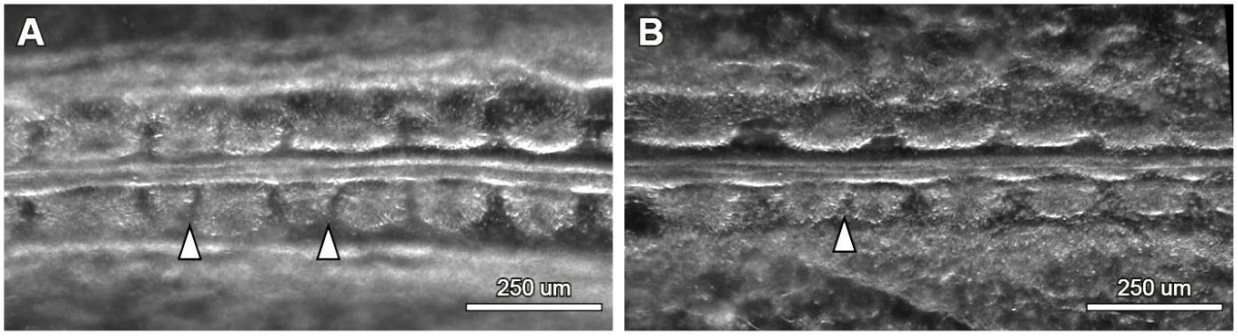

Fig. S8: Unequally sized daughter somites. Anterior is to the left. White arrowheads indicate gaps between unequal daughter somite pairs.

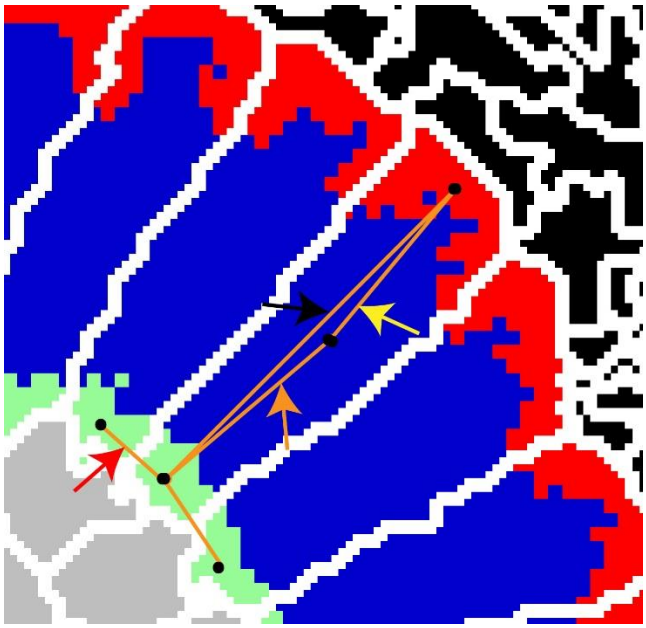

Fig. S9: Snapshot of various cell types present in the simulations. Mesenchymal cells shown in grey. Epithelial cells consist of three domains: Apical (green), lateral (blue) and basal (red) domain. Center of masses (black dots) of epithelial cell domains are connected internally to each other using elastic springs. The springs between apical and lateral domain (orange arrow), lateral and basal domain (yellow arrow) and apical and basal domain (black arrow) are indicated. Each epithelial cell has the same spring configuration helping epithelial cells to elongate after polarization. Apical domains of neighboring are also connected via springs (red arrow) to trigger the formation of single layer of epithelial cells. Black cells in the upper right-hand corner represent ECM.

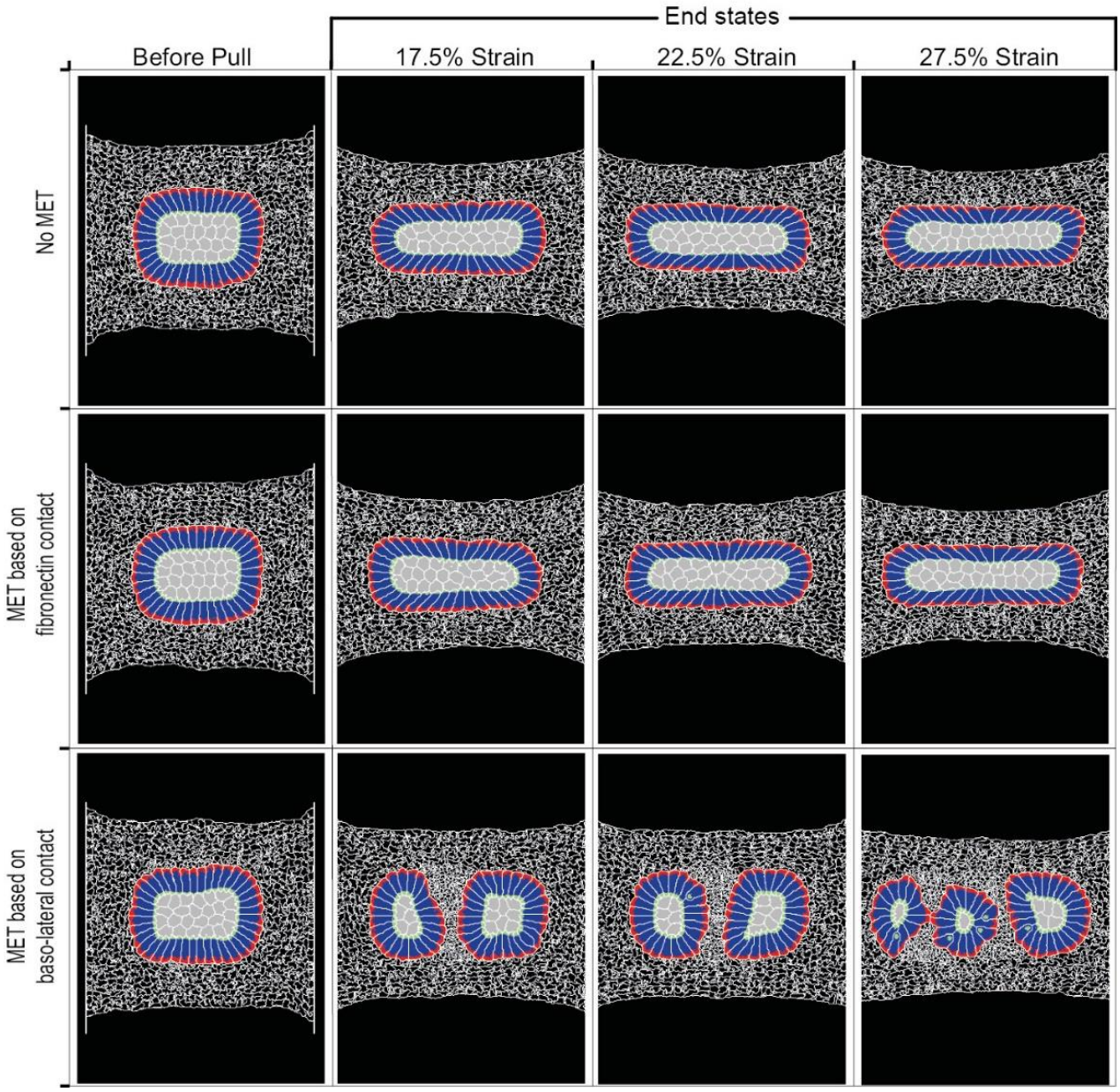

Fig. S10: End states of simulations, testing different mesenchymal-epithelialization transition rules. Fully epithelialized somites were exposed to different strains (strain given by relative change in distance between movable walls), inducing aspect ratios of 2.5 (17.5% strain), 2.9 (22.5% strain) and 3.3 (27.5%) (compare Fig. 3G). *Top row*: No MET was allowed after the pull. This was due to our initial hypothesis that somite doubling is nothing more than the reorganization of existing epithelial cells. We applied different strain values to see if high strain might lead to somite

doubling. No somite division was observed. *Middle row*: MET was allowed after the pull if a cell had been in contact to the surrounding ECM matrix for a certain period of time. This MET rule did not allow somite division under various strain conditions. *Bottom row*: A new rule allows MET of mesenchymal cells upon contact to the lateral or basal membranes of epithelial cells. Formation of stable daughter somites could be observed. Both, ECM (fibronectin) induced epithelialization and basolateral contact induced epithelializing were sufficient to generate fully epithelialized somite-like structures prior to stretching.

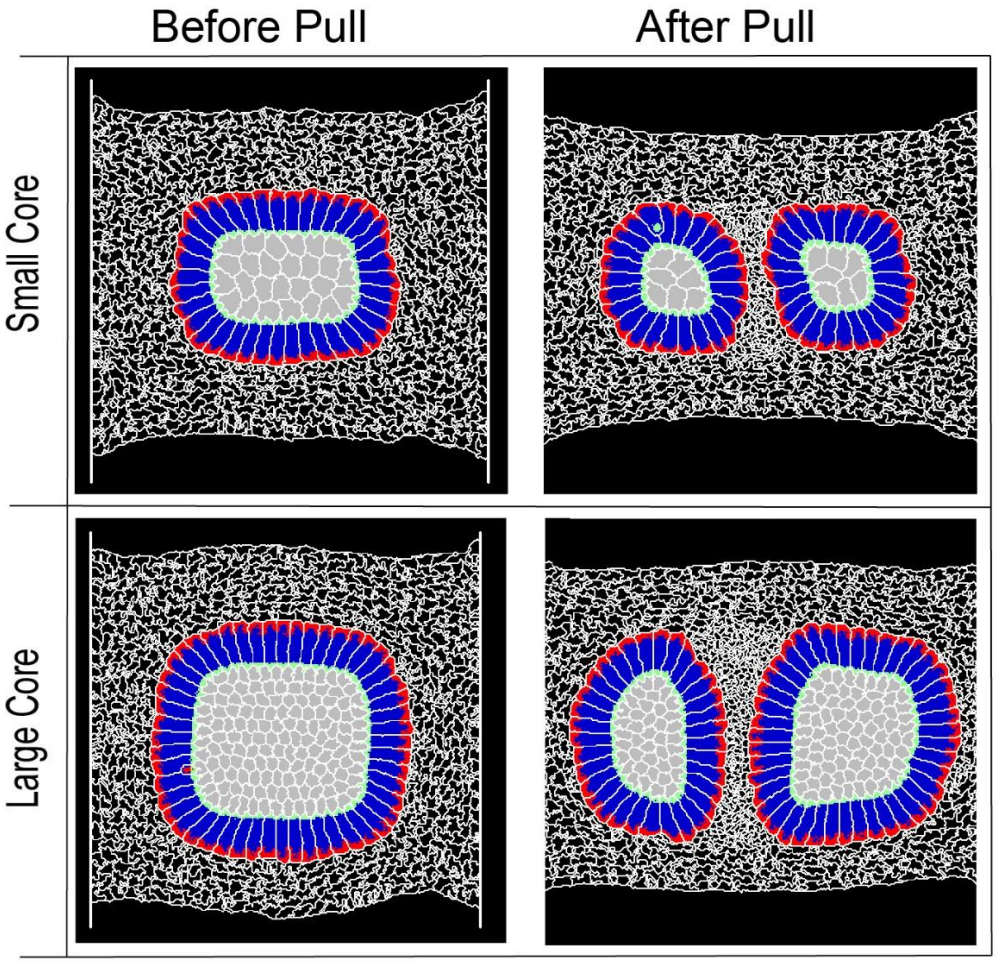

Fig. S11: Different somite core sizes and mesenchymal cell sizes. *Top row:* Small core somite before and after pull showing somite divisions after pull. Similar response of somite division can also be seen in the large core somite (*Bottom row*). This in silico model of somite division also allows to change the size of the cells. This is evident by comparing the size of the core mesenchymal cells (in grey) in the top and bottom rows.

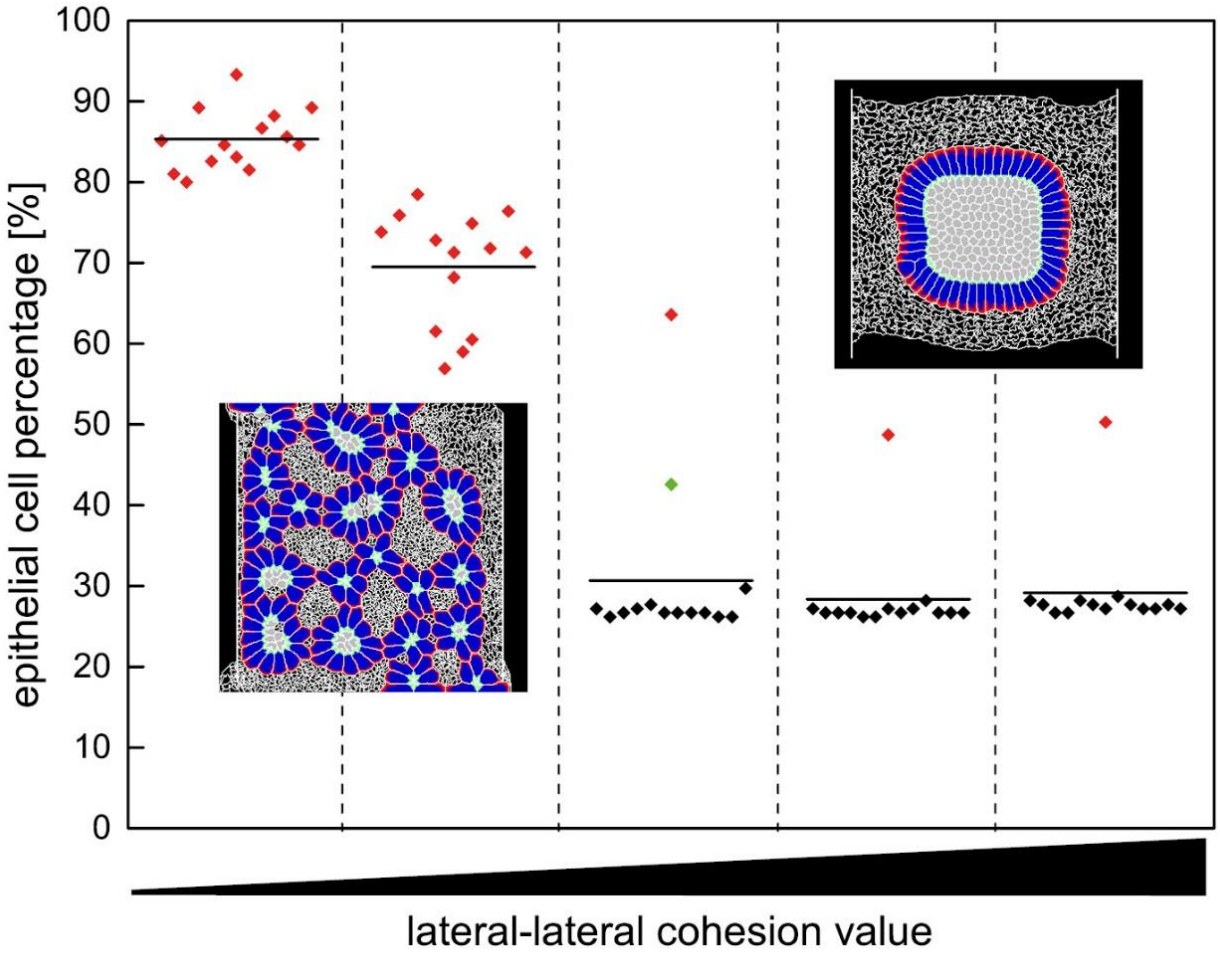

Fig. S12: Influence of cohesion between lateral domains of epithelial cells on daughter somite number and epithelial cell percentages *in silico.* Cohesion between lateral domains of epithelial cells was varied in non-stretched somites to study the effect on somite formation. With low cohesion, almost 85% of mesenchymal cells became epithelial. This increase in epithelial cell number resulted in the formation of many epithelialized cell clusters (red data points), whereas for high cohesion values, we observed no somite division except for one case (green data point). Non-dividing somites are indicated by black data points.

S1 Table: Mechanical strain caused by application of the external mechanical pull.

Daughter somite formation?	Embryo No.	Distance per pull [mm]	Mechanical Strain [%]	
			pull 1	pull 2
yes	1	3.85	21	19
	2	3.8	21	20
	3	3.7	21	20
	4	3.85	26	16
	5	3.85	26	21
	6	3.85	21	17
	7	3.85	26	15
	8	3.85	25	17
	9	3.85	26	15
	10	3.9	27	24
	11	3.95	28	19
	12	3.95	18	20
	13	3.95	24	22
	14	3.95	22	18
	15	3.95	20	19
	16	3.95	22	15
no	17	3.85	23	19
	18	3.8	22	18
	19	3.85	21	19
	20	3.85	25	13
	21	3.7	18	17

S2 Table: Somite formation rates for stretched embryos, with and without daughter somite formation, and control embryos.

Daughter somite formation?	Embryo No.	Somite No. initial	Somite No. final	Time interval [min]	Somite formation rate [min/somite]
YES	1	10	18	610	76.3
	2	9	19	785	78.5
	3	14	22	636	79.5
	4	14	20	498	83.0
	5	13	20	618	88.3
	6	14	21	536	76.6
	7	14	20	520	86.7
	8	12	19	524	74.9
	9	13	21	584	73.0
	10	6	13	565	80.7
	11	12	17	451	90.2
	12	17	24	556	79.4
	13	15	24	723	80.3
	14	15	21	510	85.0
	15	15	22	553	79
	16	17	25	523	65.4
				Average ± Stdev.:	**79.8 ± 6.2**
NO	17	15	22	578	82.6
	18	11	21	795	79.5
	19	17	23	413	82.6
	20	15	21	510	85
	21	12	22	826	82.6
				Average ± Stdev.:	**82.5 ± 2.0**
Controls	22	6	12	527	87.8
	23	6	23	1301	76.5
	24	7	20	915	70.4
	25	8	21	1079	83
				Average ± Stdev.:	**79.4 ± 7.6**

S3 Table: Parameters values used in the Cellular Potts Model.

Parameter	Value
Simulation lattice size	400 pixels x 300 pixels
Simulation temperature (Noise)	100
Total simulation steps	130000 Monte Carlo steps (MCS)
Moment pull	60000 MCS
Pull duration	10000 MCS
Epithelial target volume V_{epi}	300 pixel (9% Apical, 70% Lateral and 21% Basal)
Epithelial volume stiffness $\lambda_{volume-\ epi}$	100
Mesenchymal volume V_{mes}	195 pixels
ECM volume stiffness $\lambda_{volume-\ mes}$	30
ECM cell volume V_{ecm}	75 pixels
ECM volume stiffness $\lambda_{volume-\ ecm}$	25
Epithelial polarization time	1500 MCS
Epithelial elongation time	1500 MCS
Epithelial sub-cellular units spring stiffness	500
Apical – Lateral spring length	15 pixels (absolute distance between center of masses of two cells)
Apical – Basal spring length	30 pixels (absolute distance between center of masses of two cells)
Lateral – Basal spring length	20 pixels (absolute distance between center of masses of two cells)
Apical – Apical spring stiffness	100
Apical – Apical spring length	4 pixels (absolute distance between center of masses of two cells)
ECM - ECM spring stiffness	200
ECM – ECM spring length	10 pixels (absolute distance between center of masses of two cells)
Contact Energies	
Inter-cellular (external) adhesion energies	
$J_{med-apical}$, $J_{med-lateral}$, $J_{med-basal}$, $J_{med-mes}$, $J_{med-ecm}$,	300, 300, 300, 300, 30
$J_{apical-apical}$, $J_{apical-lateral}$, $J_{apical-basal}$, $J_{apical-mes}$, $J_{apical-ecm}$	3, 150, 150, 10, 160
$J_{lateral-lateral}$, $J_{lateral-basal}$, $J_{lateral-mes}$, $J_{lateral-ecm}$,	70, 100, 200, 130
$J_{basal-basal}$, $J_{basal-mes}$, $J_{basal-ecm}$	30, 280, 40
Internal adhesion energies (between domains)	
$J_{apical-lateral}$, $J_{apical-basal}$, $J_{lateral-basal}$	2, 20, 2

Movie S1: Control embryo

Time-lapse movie of the development of a control chick embryo (stage HH9+), cultured ex ovo, mounted in submerged filter paper sandwiches in the stretch setup for 19 hours, without stretching. Timer is in hours.

Movie S2: Stretched embryo showing somite divisions

Time-lapse movie of the development of an experimental chick embryo (stage HH10), cultured ex ovo, mounted in submerged filter paper sandwiches in the stretch setup for 17,5 hours, and stretched at a speed of 1.2 µm/s along the anterior-posterior (AP) axis, in two pulls. First the overview is shown, afterwards a zoom in at the mesoderm. The stretching deforms the embryos slowly but substantially, while development progresses without damage. During the deformation, somites divide into daughter somites of different sizes, as marked by the white arrowheads in the zoom. For example: the first arrowhead shows an asymmetric somite division (lower left), while the second arrowhead shows a symmetric division (upper left).

Movie S3: Somite epithelialization and division *in silico*.

Simulation video of dividing *in silico* somites, consisting out of frames of every 500th Monte Carlo Step. We tested different rules in our Cellular Potts model concerning cellular behavior in the deformed somites, to find out the most likely mechanism for the somite division to take place. Daughter somite formation in stretched somites could only successfully be induced when a MET of mesenchymal core cells upon contact to the basal or lateral membranes of epithelial cells was allowed.